

Magnetic dichroism in valence band photoemission

Wolfgang Kuch¹ and Claus M Schneider²

¹ Max-Planck-Institut für Mikrostrukturphysik, Weinberg 2, D-06120 Halle, Germany

² Institute for Solid State and Materials Research IFW Dresden, Helmholtzstrasse 20, D-01069 Dresden, Germany

E-mail: kuch@bessy.de (W Kuch) and c.m.schneider@ifw-dresden.de (C M Schneider)

Received 6 September 2000, in final form 7 November 2000

Abstract

Magnetic dichroism in photoemission has matured into a versatile and indispensable spectroscopic tool in surface and thin-film magnetism. Not only in core-level investigations, but also particularly in the analysis of valence electronic states ('band mapping'), magnetic dichroism reveals its merits. It allows one to characterize in detail the role of spin-orbit coupling in the valence bands, thereby arriving at a refined picture of the electronic structure of a ferromagnet. The various forms of magnetic dichroism, the underlying physical mechanisms, and selected results are discussed in a tutorial framework from an experimentalists point of view.

Contents

	Page
1. Introduction	149
2. Spin- and angle-resolved photoemission: a brief review	149
2.1. Spin-dependent interactions in a solid	150
2.2. Optical excitation of spin-polarized photoelectrons	157
2.3. Photoemission from magnetic materials	162
3. Geometrical considerations: a qualitative approach based on symmetry arguments	163
4. Selected experimental results	167
4.1. Normal emission, circular polarization, perpendicular magnetization	168
4.2. Normal emission, linear polarization, in-plane magnetization	185
4.3. Normal emission, circular polarization, in-plane magnetization	193
4.4. Off-normal emission	194
5. Outlook	202
Acknowledgments	202
References	202

1. Introduction

During the last 20 years our basic understanding of ferromagnetism and magnetic phenomena has considerably improved. This is mainly due to the progress in the quantum mechanical treatment of many-electron systems by *ab initio* approaches. Aspects which earlier on could only be treated within perturbational approximations in the framework of a Schrödinger equation—for example, the influence of spin–orbit coupling [1]—nowadays are incorporated into fully relativistic computational schemes solving the appropriate Dirac Hamiltonian [2–4].

This progress in solid-state theory was accompanied by the development of new spectroscopic techniques in order to meet the challenge of testing new band-structure calculations. The continuously improving access to synchrotron radiation with its particular properties, such as high flux, tunability, and polarization characteristics, played and still plays an important role in this process. Only through synchrotron-radiation-based electron spectroscopies has it become possible to investigate the electronic structure of magnetic materials in finer and finer detail. Milestones in this field were set by the first spin- and angle-resolved photoemission experiments in 1981 [5,6], the discovery of magnetic dichroism in x-ray photoabsorption [7,8], and the observation of magnetic dichroism in spin-integrated and spin-resolved photoemission at the beginning of the 1990s [9,10].

In particular, magnetic dichroism in valence band photoemission has been demonstrated to yield a detailed insight into the electronic structure of ferromagnetic surfaces and thin films. The experiments can be performed with commercial electron spectrometers and detectors. The technique represents the counterpart to explicitly spin-resolving approaches, which generally require specialized equipment and are very time consuming. In many—but not all—cases, magnetic dichroism measurements may yield similar information to spin-resolved experiments—in particular, if the former are backed up by fully relativistic photocurrent calculations.

In our contribution we review the fundamental aspects and the current status of magnetic dichroism in valence band photoemission. In view of the experimentalist's need, emphasis is put on the educational aspects. We therefore choose a symmetry-based rather than a computational approach when introducing the reader to the quantum mechanical mechanisms which underlie magnetic dichroism. It turns out that within this framework a large amount of information on the electronic structure of the system under investigation can already be extracted from experimental data. For the sake of clarity, the main focus will be on the explanation of experimentally observed effects in terms of three-dimensional electronic band structure. No attempt will be made here to account for quantization in one direction introduced by finite-size effects. In a case where these effects become important, e.g., for film thicknesses in the monolayer limit, the underlying quantum mechanical description is basically the same, but numerical calculations will be needed to input a properly quantized electronic structure.

2. Spin- and angle-resolved photoemission: a brief review

Magnetic dichroism is an intricate physical phenomenon. It requires the electronic structure to have two specific properties: (i) the ground state of the electronic system must be spin polarized; (ii) the electronic wavefunctions must be subject to a non-vanishing spin–orbit coupling. The first precondition implies the electron spins to have a defined spatial orientation. In a ferromagnetic material this orientation is given by the direction of the macroscopic magnetization $\vec{M}(\vec{r})$. It may change throughout the sample as a function of the spatial coordinates \vec{r} corresponding to a magnetic domain pattern. The quantum mechanical origin of the magnetic state is the exchange interaction. As we will see in more detail below, the

second precondition couples the electron spin to the orbital part of the wavefunction and thus to the crystal lattice. We therefore have two different interactions—a ‘magnetic’ and a ‘non-magnetic’¹ one—connecting the electron spin to the three-dimensional space.

The fundamental principle underlying the phenomenon of magnetic dichroism is the spin-dependent optical excitation of electrons. In a single-electron model this process leads to a spin-polarized electron in the final state. If the final state lies above the vacuum level E_{vac} , the electron may be analysed outside the crystal by means of an appropriate experimental technique, namely spin-resolved photoelectron spectroscopy. The photoelectrons are usually monochromatized using an electron spectrometer, and subsequently enter a spin polarimeter. In this way, one obtains both intensity and spin-polarization spectra in a single measurement. For details on the various technical aspects of spin-polarized photoelectron spectroscopy and spin polarimeters, the reader is referred to comprehensive reviews [11, 12].

It is important to point out that each of the above-mentioned interactions by itself can be exploited to generate spin-polarized electrons in an appropriate photoemission experiment. From these spin-polarized electrons, a wealth of information about the particular electronic structure and the influence of the relevant spin-dependent interaction on this electronic structure can be inferred. The physical mechanisms giving rise to spin-polarized photoelectrons for the two cases of spin-orbit coupling and exchange interaction, however, differ considerably in detail. As a first step in our approach to the phenomenon of magnetic dichroism, we will therefore discuss the case of spin-orbit coupling and spin-polarized photoemission from non-magnetic materials. The quantum mechanical process governing this case is also called ‘optical spin orientation’. As we will show in section 3, the concept of optical spin orientation can be generalized to magnetic materials where it is called magnetic dichroism.

In the following we first focus our attention on the quantum physical mechanisms which are employed when optically orienting the photoelectron spin in non-magnetic materials.

2.1. Spin-dependent interactions in a solid

2.1.1. Formal description of a single-electron system. In order to comprehend the implications for the electronic structure in a solid brought about by the electron spin, it is instructive to start from an elementary (non-relativistic) level of quantum mechanics. In such a textbook situation, the electron moving in an electrostatic potential $V(\vec{r})$ may be described by the (time-independent) Schrödinger equation

$$\mathcal{H}|\phi(\vec{r})\rangle = [\mathcal{T} + V(\vec{r})]|\phi(\vec{r})\rangle = \left[\frac{\hat{p}^2}{2m} + V(\vec{r}) \right] |\phi(\vec{r})\rangle = E_{n,\ell}|\phi(\vec{r})\rangle. \quad (1)$$

The Hamiltonian \mathcal{H} acting on the electron wavefunctions $\phi_{n,\ell} = |n, \ell\rangle$ contains the momentum operator \hat{p} (via the kinetic energy operator \mathcal{T}) and the potential. In the case of a solid, $V(\vec{r})$ is a periodic potential reflecting the symmetry of the crystal lattice, and the electronic states are becoming Bloch states $|n, \Gamma^\delta, \vec{k}\rangle$ with a wavevector \vec{k} . Note that the atomic angular momentum ℓ is no longer a good quantum number of the solid, because the crystal field breaks the spherical symmetry. As a consequence, states with different ℓ -values hybridize (e.g., sp or spd hybridization). Nevertheless, when discussing specific properties of electronic

¹ This distinction is clearly a phenomenological one. It relates the individual spin-dependent interactions to the type of material in which their presence can be most easily observed by spin-resolved photoemission experiments. The effects of spin-orbit coupling can be studied best in non-magnetic materials, whereas the observation of spin-polarization effects due to exchange interaction requires the experiments to be carried out on a ferromagnetic system. One should keep in mind that in a microscopic picture, both spin-orbit and exchange coupling are caused by electrostatic interactions.

bands, one often finds—sometimes misleading—references to the corresponding atomic state character denoted by ℓ ('d'- or 'f'-like bands). Both the eigenfunctions $|n, \Gamma^\delta, \vec{k}\rangle$ and the energy eigenvalues $E_{n,\vec{k}}$ are distinguished by quantum numbers n and \vec{k} . A full set of energy eigenvalues forms the band structure $E_n(\vec{k})$ of the solid with the band index n and the electron wavevector \vec{k} . Note that the wavefunctions are further classified by the so-called irreducible representations Γ^δ of the crystal's symmetry group (see section 2.1.2) and depend only on the spatial coordinates \vec{r} or, equivalently, the wavevector \vec{k} .

Any electronic state is marked by a full set of quantum numbers which must therefore also include the electron spin. Formally, the respective states will be written as $|n, \Gamma^\delta, \vec{k}, s\rangle$. However, as long as the Hamiltonian acts only on the spatial part of the wavefunction (as in equation (1)), $|n, \Gamma^\delta, \vec{k}, s\rangle$ is conveniently separated into independent spatial and spin parts:

$$|n, \Gamma^\delta, \vec{k}, s\rangle = |n, \Gamma^\delta, \vec{k}\rangle |s\rangle. \quad (2)$$

Clearly, any explicit spin effects in the electronic structure can only arise if further interactions are included in the Hamiltonian. When starting from equation (1) this is a somewhat artificial process. We must therefore switch to a higher level of sophistication. The electron spin can be adequately treated only within the framework of relativistic quantum mechanics. In this case the problem of electrons moving in an electromagnetic field is described by the Dirac equation. This formalism is rigorously employed in contemporary electronic structure calculations, with the appropriate wavefunctions being four-component spinors Ψ . From the didactic point of view, however, a Dirac spinor is not exactly a lucid entity if it comes to the discussion of electronic wavefunctions. Whenever applicable, one thus tries to reduce the problem to a more manageable form. Provided that the kinetic and potential energies of the particles are both small compared to mc^2 , the Dirac equation can be treated in the non-relativistic limit. Two components of Ψ are negligibly small and one ends up with two-component spinors Φ as defined in equation (4). The resulting mathematical description of a *single-electron system* is known as the Pauli equation:

$$\left(\underbrace{\frac{1}{2m} \left(\vec{p} - \frac{e}{c} \vec{A} \right)^2}_{\mathcal{H}_0} + eV(\vec{r}) - \underbrace{e \frac{e\hbar}{2mc} \vec{\sigma} \cdot \vec{B}}_{\mathcal{H}_B} + i \underbrace{\frac{e\hbar}{4m^2c^2} \vec{E} \cdot \vec{p}}_{\mathcal{H}_D} - \underbrace{\frac{e\hbar}{4m^2c^2} \vec{\sigma} \cdot (\vec{E} \times \vec{p})}_{\mathcal{H}_{so}} \right) \Phi = E\Phi \quad (3)$$

with

$$\Phi = \varphi_a(\vec{r}) |\uparrow\rangle + \varphi_b(\vec{r}) |\downarrow\rangle. \quad (4)$$

The first term \mathcal{H}_0 basically contains the simple Hamiltonian in (1) and also accounts for the vector potential A of the magnetic field. \mathcal{H}_0 also reflects the symmetry properties of the electronic system. The Darwin term \mathcal{H}_D can be understood as a relativistic energy correction to the electron energy. Inclusion of \mathcal{H}_D does not change the symmetry of the system described by the Hamiltonian \mathcal{H}_0 . This is an important difference from the case for the remaining contributions \mathcal{H}_B and \mathcal{H}_{so} which will be dealt with in the following.

\mathcal{H}_B contains the interaction between the electron spin $\vec{\sigma}$ and a magnetic field \vec{B} . \vec{B} does not fulfil the symmetry property of time reversal and \mathcal{H}_B consequently destroys the time-reversal symmetry within the electron system. This causes a field-induced splitting of previously degenerate energy levels in the sense of a Zeeman effect. We must emphasize that \mathcal{H}_B does *not* describe the situation in a ferromagnet, as equation (3) was derived for a single-electron system. Ferromagnetism and the corresponding spin-dependent level splitting arise due to exchange and correlation in a *many*-electron system. These correlation effects can be properly accounted for only in a many-electron approach as, for example, in density

functional theory. The density functional treatment of the many-electron problem leads to a set of single-electron (Kohn–Sham) equations in which exchange and correlation effects are contained in a potential $V_{exc}^{\uparrow\downarrow}(\vec{r})$. This so-called exchange and correlation potential leads to a spin-dependent contribution \mathcal{H}_{ex} to the single-electron Hamiltonian. In the simplest case of a Stoner–Wohlfarth-type model, this term corresponds to a quantity

$$\mathcal{H}_{ex} = \pm e V_{exc}^{\uparrow\downarrow}(\vec{r}). \quad (5)$$

This is the quantum mechanical origin for ferromagnetism and the associated band splitting. The plus and minus signs correspond to the potentials for $|\uparrow\rangle$ and $|\downarrow\rangle$ electrons, respectively. Including the exchange term changes equation (3) to

$$\mathcal{H} = \mathcal{H}_0 + \mathcal{H}_B + \mathcal{H}_D + \mathcal{H}_{so} + \mathcal{H}_{ex}. \quad (6)$$

Another important property of \mathcal{H}_B is the connection between spin and real space, because the spin aligns itself along the quantization axis defined by the direction of the magnetic field vector. It is important to recognize that the exchange contribution \mathcal{H}_{ex} by itself does *not* provide this coupling between spin and real space. It causes, however, a spontaneous magnetization $\vec{M}(\vec{r})$ which takes the role of a magnetic field in its effect on the electronic system. The terms \mathcal{H}_B and \mathcal{H}_{ex} and their symmetry-breaking properties must therefore be considered as a single entity.

The last term in equation (3), \mathcal{H}_{so} , also connects the spin to the three-dimensional space, but through a different mechanism, namely the spin–orbit interaction. It couples the spin and orbital parts of the electronic wavefunctions and is basically an atomic property. According to Bassani and Parravicini [13], the Hamiltonian \mathcal{H}_{so} in a crystalline system with the electrostatic potential $V(\vec{r})$ takes the form²

$$\mathcal{H}_{so} = \frac{e\hbar}{4m^2c^2} \vec{\sigma} \cdot (\vec{\nabla}V(\vec{r}) \times \vec{p}). \quad (7)$$

The term \mathcal{H}_{so} lowers the symmetry of the quantum mechanical problem. It will give rise to the lifting of degeneracies and cause electronic states to split in energy. The wavefunction itself becomes a two-component spinor and usually contains a linear combination of the two spin characters.

2.1.2. The role of symmetry. The symmetry properties of a solid—or rather the electrostatic potential $V(\vec{r})$ —are reflected in the electronic structure. A particularly important quantity is the symmetry character of an electronic state. It can be used to treat optical interband transitions in the electronic structure of a solid by means of dipole selection rules.

The symmetry operations leaving a point in the elementary cell of the lattice invariant form a point group \mathbf{G} . This point group can be unambiguously described by a set of so-called irreducible representations Γ^δ . The corresponding electronic states are classified according to these irreducible representations, and form a basis set. For the three axes of highest spatial symmetry in a cubic crystal, [100], [110], and [111], corresponding to the directions Δ , Σ , and Λ in the bulk Brillouin zone, the irreducible representations are denoted as given in table 1.

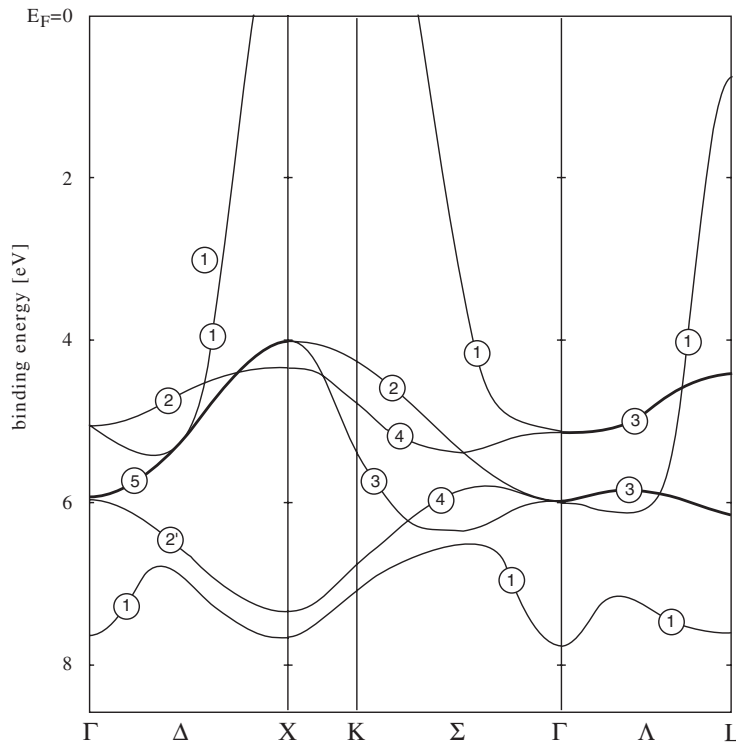
The above irreducible representations are also called single-group representations. They take into account only the spatial symmetries in the system and are used to distinguish the various electronic bands along a high-symmetry direction. Please note that contrary to traditional practice we use superscripts to distinguish the representations. This notation is more convenient if we want to expand the formalism to include magnetic materials. The marked (\triangleleft)

² Equation (7) is not restricted to a periodic potential, but remains valid for any potential arising from the interaction with charges.

Table 1. Non-relativistic irreducible representations for electronic states along the three high-symmetry directions in a cubic crystal. The symbol \triangleleft marks two-dimensional representations.

[100]	[110]	[111]
Δ^1	Σ^1	Λ^1
$\Delta^{1'}$	Σ^2	Λ^2
Δ^2	Σ^3	$\Lambda^3_{\triangleleft}$
$\Delta^{2'}$	Σ^4	
Δ^5_{\triangleleft}		

representations are two dimensional, i.e., describe an electron level which is doubly degenerate with respect to the energy eigenvalue. In addition, every electronic state is doubly degenerate with respect to the electron spin. This is known as Kramers degeneracy. As an example, we reproduce the band structure of Ag along three principal directions Γ -X, Γ -K, and Γ -L in figure 1. The bands are numbered according to the single-group representation along the respective direction.

**Figure 1.** Non-relativistic energy bands in Ag. The numbers indicate the single-group labelling according to table 1. Degenerate states of Δ^5 and Λ^3 character are indicated by heavy lines.

Degenerate states of Δ^5 and Λ^3 character are indicated by heavy lines. The resulting band structure is often called non-relativistic, although it may already contain the energy renormalization due to the Darwin term.

Inclusion of spin-orbit coupling reduces the symmetry of the electronic system. This is taken into account by using a different set of irreducible representations to distinguish the

energy bands. These representations are taken from the relativistic double group \mathbf{DG} , which can be constructed from the allowed symmetry operations in the electronic system with spin-orbit coupling. Formally, the double group is obtained by multiplying the single group with the rotational group in spin space, i.e., $\mathbf{DG} = \mathbf{G} \otimes \mathbf{SU}_2$. Due to the reduced total symmetry, the number of irreducible representations of \mathbf{DG} is smaller than in the case without spin-orbit coupling (table 2).

Table 2. Relativistic irreducible representations for electronic states along the three high-symmetry directions in a cubic crystal.

[100]	[110]	[111]
Δ_6	Σ_5	Λ_6
Δ_7		$\Lambda_{4,5}$

In order to distinguish single- and double-group representations, the latter are denoted by subscripts. Most of the double-group representations are one dimensional, with two exceptions along Λ : (i) the notation $\Lambda_{4,5}$ stands for two single-valued representations Λ_4 and Λ_5 , which are degenerate by time-reversal symmetry; (ii) the representation Λ_6 is two dimensional. The single-valued representations in table 1 are unambiguously connected with the double-group representations in table 2. This is explained in table 3. For each of the three high-symmetry directions in a cubic crystal the double-group representation which results from the respective single-group representation on multiplying with the spin representation Δ_6 is shown by the subscript. In the presence of spin-orbit coupling, the single-group symmetry is no longer a good quantum number. At each point in k -space each band can be composed by a linear combination of different single-group representations. However, for vanishing spin-orbit coupling the bands have to be of pure single-group symmetry. Since the non-relativistic dipole selection rules remain valid, and only transitions between bands with an admixture of the allowed single-group symmetries are possible, we will keep the predominant single-group representation of each band as a superscript in labelling whenever practical, hereby following the nomenclature of reference [14]. We will refer to the predominant single-group symmetry as the ‘spatial symmetry’.

Table 3. The connection between non-relativistic and relativistic representations. For each of the three high-symmetry directions in a cubic crystal, the non-relativistic single-group representations are displayed in the left-hand column. The resulting relativistic double-group symmetry in the presence of spin-orbit coupling is shown in the right-hand column (subscripts). Superscripts denote the predominant single-group symmetry (‘spatial symmetry’). The twofold-degenerate single-group representations Δ^5 and Λ^3 split into Δ_6^5, Δ_7^5 and $\Lambda_{4,5}^3, \Lambda_6^3$, respectively.

	[100]	[110]	[111]
Δ^1	Δ_6^1	Σ^1	Σ_5^1
$\Delta^{1'}$	$\Delta_6^{1'}$	Σ^2	Σ_5^2
Δ^2	Δ_7^2	Σ^3	Σ_5^3
$\Delta^{2'}$	$\Delta_7^{2'}$	Σ^4	Σ_5^4
Δ^5	Δ_6^5		
	Δ_7^5		

The degeneracy of the states characterized by the two-dimensional representations in table 1 is lifted. These states therefore split in energy, and are connected with both relativistic representations (if there are two available). The corresponding bands are said to be spin-orbit

split. The spin-orbit splitting depends strongly on \vec{k} and may even tend towards zero at particular points in the Brillouin zone. A special situation is found in the Σ direction, where only one-dimensional single-group representations exist, and no spin-orbit splitting occurs.

In order to see the changes in the band structure brought about by spin-orbit coupling, it is instructive to start from the non-relativistic case and follow the development of the electronic structure step by step. In the first step, we simply introduce a band splitting of the degenerate states, i.e., those marked by heavy lines in figure 1. The resulting ‘intermediate’ band structure is shown in figure 2. We assume a \vec{k} -independent splitting of the Δ^5 and the bottom Λ^3 bands. For the upper Λ^3 band the splitting varies with \vec{k} , and vanishes at the Γ point.

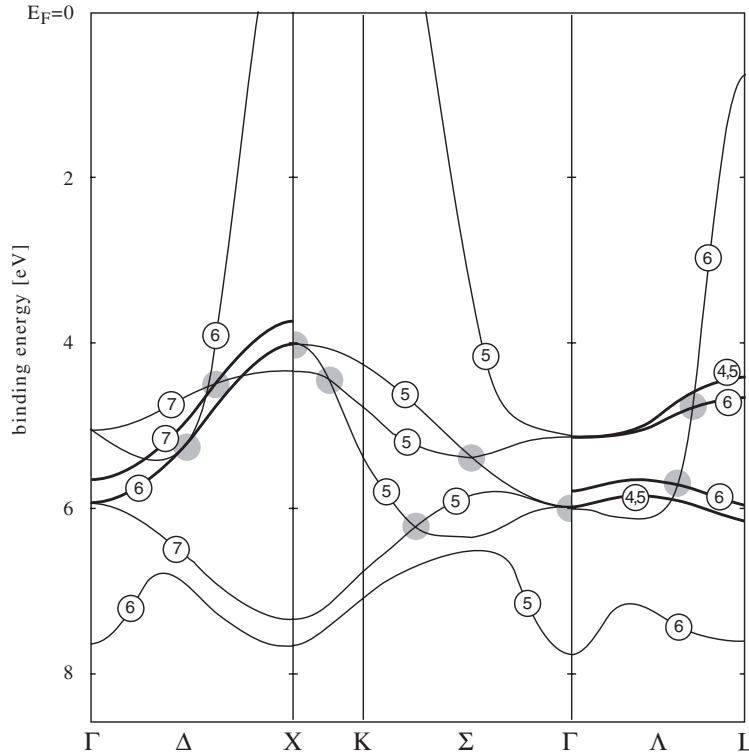


Figure 2. The intermediate step in constructing a relativistic band structure of Ag. The heavy lines indicate band splitting due to spin-orbit coupling; shaded areas mark possible hybridization points.

In the next step, we must identify hybridization points in our hypothetical band scheme. For this purpose the bands must be labelled with their proper double-group representations. This is done according to table 3, which gives the connections between single-group and double-group representations. For the moment we will concentrate just on the double-group labels. Inspection of figure 2 reveals a number of crossing points between bands of the same double-group representation. These crossing points are marked by shaded areas. Since bands of the same symmetry are not allowed to cross, spin-orbit coupling will lead to the formation of hybridization gaps at these points in the real band structure. One should also note the importance of the hybridization points at X^5 and $\Gamma^{2,5}$ on the Σ line. The Σ bands starting at these points must split in order to make contact with the spin-orbit-split Δ and Λ states arriving from the other side of the symmetry point. The connection between the symmetry

of a band and a point in the Brillouin zone is determined by compatibility relations [15]. At the high-symmetry point $\Gamma_{8^+}^{1,2}$, for example, the following bands start: Δ_7^2 , Δ_6^1 , Λ_6^3 , $\Lambda_{4,5}^3$, Σ_5^1 , and Σ_5^2 .

Now we can turn to the relativistic band structure of Ag which is displayed in figure 3. The bands are again labelled by their double-group symmetry only. To facilitate the comparison with figure 2, the approximate positions of the hybridization gaps induced by spin-orbit coupling are also indicated by shaded areas.

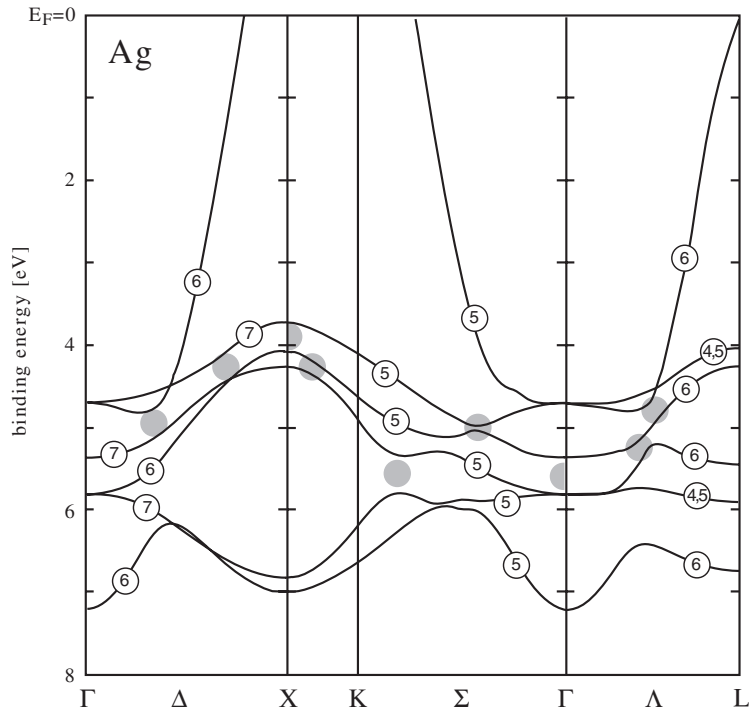


Figure 3. Calculated relativistic energy bands in Ag (after [16]). Shaded areas indicate the positions of former band crossings from figure 2.

The hybridization areas are precisely the reason that in figure 2 we refrain from including the spatial symmetry (superscripts in table 3) in the band labelling. A hybridization gap occurs if bands of the same double-group character, but with different single-group (spatial) symmetry, intersect. As a consequence, throughout a hybridization region the spatial symmetry of the band changes. In order to make this effect visible, one must determine the spatial symmetry of the electronic states from appropriate band calculations. In figure 4 we display results from calculations within the combined interpolation scheme for the Δ direction of silver. The bands are numbered according to their order at the X point with band 1 denoting the bottommost Δ_6 band. The plots give the fraction of a particular spatial symmetry contributing to a band as a function of the wavevector along the Δ direction. These data show clearly that spin-orbit coupling affects *every* band in the silver band structure to a greater or lesser degree. The strongest effect is found in the bands 4 and 6, where the spatial character changes between Δ^2 and Δ^5 along the bands. This corresponds to the hybridization region close to X as marked in figure 3. It is important to understand the nature of these hybridization regions in order to be able to interpret the spin-resolved photoemission data in detail.

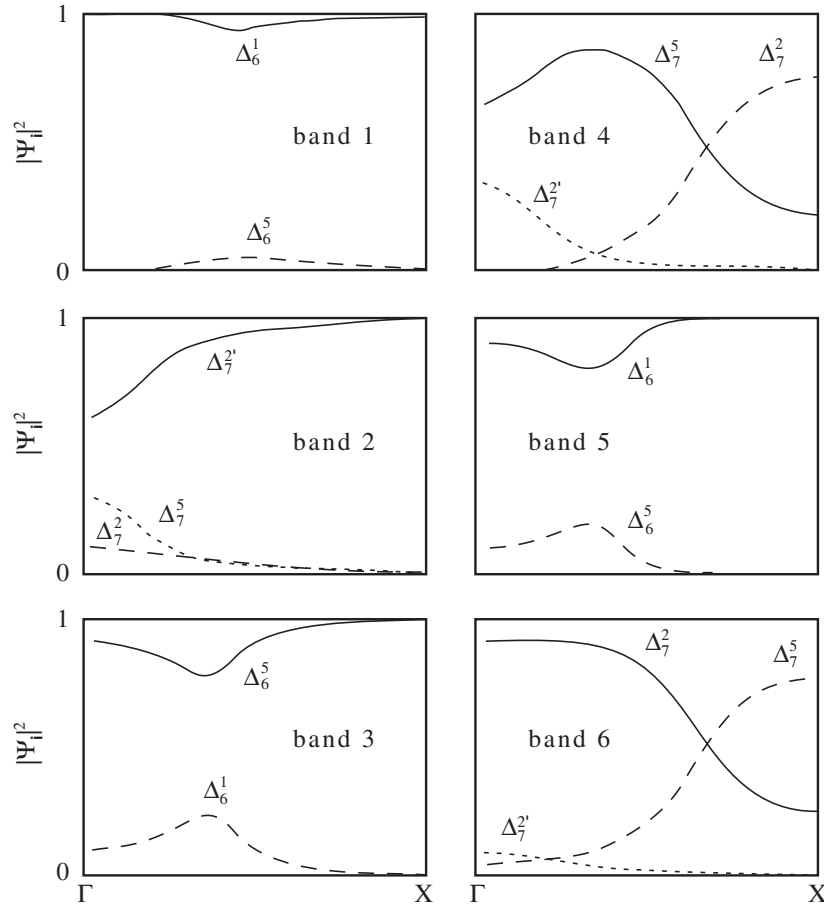


Figure 4. Relativistic electronic states in Ag along the Δ direction. Plotted is the fraction of a particular spatial symmetry contributing to a band as a function of the wavevector along the Δ direction. The numbering of the bands is according to their order at the X point with band 1 denoting the bottommost Δ_6 band. (From reference [17].)

2.2. Optical excitation of spin-polarized photoelectrons

A photoelectron emitted from a non-magnetic material with sufficiently large spin-orbit coupling will in general be spin polarized. This may seem surprising at first glance. The spin-orbit interaction, however, introduces several spin-dependent mechanisms which act in the photoemission process. As it turns out, there exist only few experimental geometries and conditions in which the emitted photoelectrons can be expected *a priori* to be unpolarized. Relativistic one-step photoemission calculations have been developed nowadays to a degree of sophistication that enables an almost quantitative comparison between theory and experiment in some cases. Unfortunately, these calculations are often not directly available for the particular system under investigation. In addition, the individual mechanisms playing a part in the photoemission process are more difficult to explain on the basis of a one-step formalism—which is an inherent property, of course. Despite its limitations, the three-step model of photoemission is often more suitable for elucidating the origin of the various spin-dependent mechanisms. We therefore start with this approach.

2.2.1. The three-step model of photoemission. The three-step model divides the photoemission process into: (i) optical excitation, (ii) transport of the excited electron through the solid, and (iii) transmission through the surface, and may thus generate magnetic dichroism. In principle, each of these three steps can depend on the electron spin. The transport polarization associated with step (ii), however, vanishes in non-magnetic centrosymmetric crystals, and will therefore be omitted from further discussions. In a one-electron model the optical excitation is often connected with the ‘initial state’, whereas the transmission of the excited electron through the surface is associated with the ‘final state’. In analogy, one may distinguish spin-dependent effects related to the initial and final states. We will first concentrate on the initial-state effects.

The optical excitation in a solid takes place via interband transitions between many-electron states $|\Psi^N\rangle$, the probability of which is described by Fermi’s golden rule:

$$I(E_i, E_f, h\nu) \sim |\langle \Psi_i^N | \mathcal{O} | \Psi_f^N \rangle|^2 \delta(E_f^N - E_i^N - h\nu). \quad (8)$$

The subscripts i and f denote the initial state and final state of the many-electron system, respectively. The operator \mathcal{O} contains the optical excitation, which is usually treated within the dipole approximation:

$$\mathcal{O} \sim \vec{A} \cdot \vec{p} \quad \text{or alternatively} \quad \mathcal{O} \sim \vec{e} \cdot \vec{r} \quad (9)$$

where \vec{e} denotes the polarization vector of the electric field.

The experimental results are often interpreted on the basis of bulk band-structure calculations. These calculations most often refer to the ground state of an effective single-electron system. Therefore, the many-particle approach in equation (8) is approximated by a single-particle picture which leads to a similar expression for the photocurrent $I(h\nu)$:

$$I(h\nu) \sim \sum_{i,f} |\langle \Phi_f | \mathcal{O} | \Phi_i \rangle|^2 \delta(E_f - E_i - h\nu) = \sum_{i,f} |M_{fi}|^2 \delta(E_f - E_i - h\nu). \quad (10)$$

The single-electron states $|\Phi_i\rangle$ and $|\Phi_f\rangle$ are Pauli spinors as defined in equation (4). The advantage of this single-particle approach is that it allows a *qualitative* interpretation of spin-integrated and spin-resolved photoemission spectra. This is done by evaluating the transition matrix elements M_{fi} on the basis of dipole selection rules. These selection rules involve solely the spatial symmetry character of the initial- and final-state wavefunctions and have been formulated for several experimental geometries in spin-integrated photoemission. They are often referred to as non-relativistic selection rules. Of particular importance is the so-called *highly symmetric arrangement* involving normally incident light and photoelectrons emitted along the surface normal \vec{n} .

The extension of the above situation to include the photoelectron spin polarization leads to the so-called relativistic selection rules. They form the basis for the mechanism of *optical spin orientation*. Just as in the non-relativistic case, the electric field in the dipole operator can act only on the spatial part of the spinor wavefunction $|\Phi\rangle$. It is important to realize, however, that the $|\uparrow\rangle$ and $|\downarrow\rangle$ parts in the spinor in equation (4) are coupled to wavefunctions $|\varphi_i(\vec{r})\rangle$ of *different* spatial symmetry. It is therefore possible to choose the experimental conditions such that only one of the spatial wavefunctions, $|\varphi_a(\vec{r})\rangle$ or $|\varphi_b(\vec{r})\rangle$, is selectively excited. Since the electron spin is preserved during the optical interband transition, we obtain spin-polarized photoelectrons in the final state. The relativistic selection rule describing this spin-selective excitation process³ relates the symmetry character of the initial- and final-state wavefunctions to the spin polarization in the final state.

The experimental conditions required for the relativistic selection rules to apply involve the above-mentioned highly symmetric arrangement and circularly polarized light. The latter

³ This process is sometimes also called optical pumping.

takes the role of the spin-quantization axis. The group theoretical analysis of the problem yields further symmetry requirements. First, the spin-polarization vector has a non-zero component only along the surface normal, i.e., $\vec{P} = (0, 0, P_z)$. Second, a reversal of the light helicity σ from left (σ^+) to right circularly polarized (σ^-) or vice versa also reverses the spin polarization:

$$\sigma^+ \rightarrow \sigma^- \longrightarrow P_z \rightarrow -P_z. \quad (11)$$

The relativistic selection rules have been derived for a number of high-symmetry axes in cubic and hexagonal crystals [14]. They have been used in a variety of experiments to investigate the influence of spin-orbit coupling on the electronic structure of high- Z (Pt, Au, etc) and low- Z (Cu, Si, etc) materials. Along the Δ and Λ lines the photoelectron spin polarization is primarily related to the excitation from spin-orbit-split bands (table 4). On the Σ line the situation is more complicated, as the spin-orbit coupling splits bands only at the zone centre and boundary. The main contribution to the optical spin orientation comes from a spin-orbit-induced hybridization of the various Σ_5 states. Due to the experimental geometry, the final state must also be of high symmetry, i.e., Δ_6^1 and Λ_6^1 , respectively. It should be noted again that because of spin-orbit coupling neither the spatial symmetry nor the spin $|\uparrow\rangle$ or $|\downarrow\rangle$ are good quantum numbers. The transition rules of table 4 are valid only for the *proportion* of bands with the respective spatial symmetry, indicated by the superscript.

Table 4. Relativistic selection rules for right-hand circularly polarized light. For left-hand circularly polarized light, $|\uparrow\rangle$ and $|\downarrow\rangle$ have to be interchanged.

[100]	[110]	[111]
$\Delta_6^5 \xrightarrow{ \downarrow\rangle} \Delta_6^1$	$\Sigma_5 \longrightarrow \Sigma_5$	$\Lambda_{4,5}^3 \xrightarrow{ \uparrow\rangle} \Lambda_6^1$
$\Delta_7^5 \xrightarrow{ \uparrow\rangle} \Delta_6^1$		$\Lambda_6^3 \xrightarrow{ \downarrow\rangle} \Lambda_6^1$

One example may suffice to demonstrate the application of the relativistic selection rules. In figure 5 we display a spin-resolved photoemission result for the Ag(001) surface which has been obtained with circularly polarized light. At the photon energy of $h\nu = 12.5$ eV the transitions take place close to the X point. The spectrum is limited to the region of the main Ag d-band emission, and shows two overlapping peaks in the total intensity. The spin polarization, however, exhibits a strong positive/negative feature, indicating that the transitions take place from spin-orbit-split bands of Δ_6^5 and Δ_7^5 double-group symmetry. From the spin polarization P and the total intensity $I = N_\uparrow + N_\downarrow$, we can calculate the so-called partial intensities which reflect the spin-up and spin-down contributions to the spectrum:

$$N_\uparrow = \frac{I}{2}(1 + P) \quad N_\downarrow = \frac{I}{2}(1 - P). \quad (12)$$

We thus see a distinct peak (A and B) in each of the partial intensity spectra in figure 5. In addition, there appears a third feature (C) in the spin-up partial intensity. This is due to a hybridization of the Δ^2 and Δ^5 spatial parts in bands No 4 and No 5 (cf. figure 4). The optical spin orientation selectively excites the Δ_7^5 contribution in band No 4, and makes the hybridization directly visible. This hybridized contribution is also responsible for the fact that the negative excursion of the spin-polarization spectrum $P_z(E)$ is smaller than the positive one. On a qualitative level the relativistic selection rules thus account well for the features in the photoemission spectrum. A quantitative interpretation, in particular, of the hybridization phenomena, however, must be based on one-step photocurrent calculations. A more detailed comparison of experiment and theory has been carried out for a number of single-crystal surfaces including Pt(111) and Cu(001) [17–20].

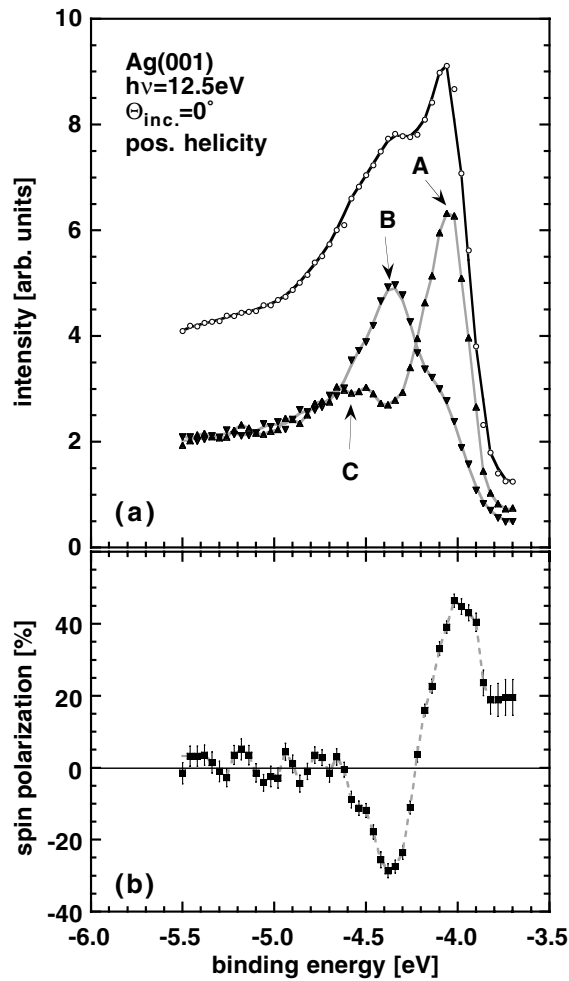


Figure 5. Spin-resolved photoemission from Ag(100). (a) Total and spin-decomposed intensity spectra (solid and grey lines, respectively) at a photon energy of $h\nu = 12.5$ eV. The features A–C correspond to interband transitions and are discussed in detail in the text. (b) The corresponding spin-polarization spectrum.

2.2.2. Beyond the three-step model: surface effects. Despite their undisputed value, the selection rules in table 4 also have a significant shortcoming. They apply strictly only to bulk electronic states, because the group theoretical derivation assumes that there is inversion symmetry. This implies a three-dimensional periodic crystal potential. In a realistic experiment, however, inversion symmetry is broken by the presence of a surface and a photoelectron detector. From the point of view of symmetry, this situation can only be adequately described by taking into account all symmetry operations leaving the *entire system*, comprising the crystal surface, and the directions of light incidence and electron emission, invariant. It is obvious that the symmetry of this system will in general be lower than that of the respective three-dimensional infinite crystal itself. This becomes particularly true for off-normal electron emission or/and light incidence. As a consequence the symmetry-enforced constraint on the spatial orientation of the spin-polarization vector \vec{P} is relaxed. Depending on the details

of the experimental geometry (including the surface crystallography), \vec{P} can have all three components non-zero [5, 21].

Another important change to our present understanding of optical orientation is brought about by the scattering properties of the surface. At the surface, the potential within the crystal changes smoothly to match the value of the vacuum level. Any photoelectron leaving the crystal will be scattered when travelling through this surface potential well, thereby changing its wavevector component k_{\perp} normal to the surface. If the scattering potential contains a contribution due to spin-orbit coupling, the scattering process itself becomes spin dependent⁴. Electrons with spin-up or spin-down character with respect to a quantization axis defined by the normal to the scattering plane are preferentially scattered into different spatial directions. This process thus acts as a ‘spin filter’: if the electrons arriving at the surface are unpolarized, i.e., the beam consists of the same number of $|\uparrow\rangle$ and $|\downarrow\rangle$ states, the *intensities* of the electron beams scattered along the two different directions are equal, but the *spin polarization* is of opposite sign [22–24]. In the case where the incident electrons are already polarized, even the intensities of the two scattered beams may differ, thereby causing a ‘dichroism’.

A final important asset beyond the limitations of the three-step model is the surface electronic structure and phenomena related to it. The surface potential step imposes boundary conditions on the electronic wavefunctions, effectively resulting in a semi-infinite electron system. This leads to the formation of surface-induced states which may be either true surface states (localized within the surface plane), surface resonances, or so-called half-space states. Their inclusion into a quantitative description of the photoemission process can only be achieved by a one-step approach which treats excitation, transport, and surface transmission within a coherent formalism. Spin-dependent effects must be taken care of by relativistic one-step photoemission calculations. This is currently the state-of-the-art position in photoemission theory.

Still, the symmetry-based approach underlying the qualitative evaluation of the transition matrix elements carries beyond the three-step model. One explicitly has to include the surface—characterized by its normal \vec{n} —in the symmetry considerations. This means that rather than the crystal symmetry alone, the symmetry of the entire system, consisting of the crystalline lattice, the surface (\vec{n}), the incident light (denoted by its wavevector \vec{q}), the electron emission direction (denoted by the electron wavevector \vec{k}), and the state of light polarization $\vec{\zeta}$, is the crucial entity. It turns out that with this extended concept of symmetry, optical spin orientation becomes possible even with linearly polarized or unpolarized light. A number of predictions for optical spin orientation from low-index surfaces with linearly polarized light have been derived from this extended symmetry concept. These predictions were supported by relativistic photoemission calculations and confirmed by a set of pioneering experiments [25–30].

The variety of optical spin-orientation mechanisms in a semi-infinite system makes the emission of spin-polarized photoelectrons a general case rather than an exception. In fact, only in particular cases can a non-zero spin polarization be ruled out on the basis of symmetry arguments. This has an important consequence for our discussion of magnetic dichroism phenomena, because magnetic dichroism is intimately connected with the spin polarization in an optical spin-orientation experiment. The following rule applies: *whenever we find a non-zero spin polarization \vec{P} in optical spin orientation from non-magnetic materials, the same experiment performed on a magnetic material will yield a magnetic dichroism, as long as the magnetization vector \vec{M} has a component along \vec{P} .*

⁴ This spin-orbit contribution to the electron scattering is particularly strong in high-Z materials such as W or Au and explains their use as targets in spin polarimeters.

2.3. Photoemission from magnetic materials

2.3.1. A non-relativistic picture. Photoelectron spectroscopy from ferromagnets was long treated within an ‘exchange-only’ picture. In particular, spin–orbit interaction was thought to be negligible for the valence states of the 3d ferromagnets Fe, Co, and Ni. Under this assumption, which corresponds to a non-relativistic picture of ferromagnetism, the lifting of the Kramers degeneracy by the exchange interaction Δ_{ex} is the decisive mechanism. Due to $\Delta_{ex}(\vec{k})$ all bands in a ferromagnet split in a \vec{k} -dependent manner into subbands of $|\uparrow\rangle$ and $|\downarrow\rangle$ spin character. This spin splitting results in an imbalance in the density of occupied spin-up (majority) and spin-down (minority) states. In turn, this imbalance is the microscopic origin of the magnetic moment or the macroscopic sample magnetization \vec{M} .

The spatial band symmetry characters (cf. table 1) are retained in the non-relativistic model since spin and spatial parts of the respective wavefunctions remain decoupled. Therefore, the set of non-relativistic selection rules can be applied to describe the optical interband transitions. For a given transition, for example of the type $\Delta^5 \rightarrow \Delta^1$, there is an excitation channel for each spin character:

$$\begin{aligned} \Delta^{5\uparrow} &\longrightarrow \Delta^{1\uparrow} \\ \Delta^{5\downarrow} &\longrightarrow \Delta^{1\downarrow}. \end{aligned} \tag{13}$$

The electron spin, with a quantization axis given by \vec{M} , is preserved during the optical transition. The polarization state ζ of the exciting radiation does not affect the photoelectron spin polarization. Because the spin polarization is already given by the spin-split initial states in the band structure, it is said to be an *initial-state effect*. The qualitative interpretation of the experimental data is relatively straightforward because the spin polarization observed can be directly related to spin-up or spin-down initial-state bands. A pioneering experiment in this field using synchrotron radiation has already been performed, in 1981 [6]. It was followed by a large number of investigations which have greatly helped to establish and refine our present understanding of ferromagnetism.

2.3.2. Relativistic ferromagnets. The situation becomes much more complex as soon as spin–orbit coupling is taken into account. Early group theoretical work by Falicov and Ruvalds indicated that the symmetry-breaking properties of the spin–orbit interaction will have serious consequences for the electronic structure [31]. First of all, spin and spatial parts of the electronic wavefunction can no longer be treated independently. This is the paramount precondition for optical spin-orientation processes. Second, the number of available irreducible representations (band symmetries) depends on the direction of \vec{M} with respect to the crystalline axes. Third, for \vec{M} lying within the surface plane, i.e., $\vec{M} \perp \vec{n}$, the number of band symmetries becomes very small, leading to a high degree of hybridization in the band structure.

The appropriate theoretical description of the electronic structure in a relativistic ferromagnet must treat exchange interaction and spin–orbit coupling on an equal footing. This is done by means of *ab initio* fully relativistic band-structure and photoemission calculations. The results from these calculations essentially supported the above predictions from group theory in detail. In addition, they proved the electron spin to lose its property of being a ‘good’ quantum number. Due to the spin–orbit-induced hybridization the spin polarization may vary along a given band *continuously* between $P = 100\%$ ($|\uparrow\rangle$) and $P = -100\%$ ($|\downarrow\rangle$). These complications must be taken into account when interpreting photoemission data from ferromagnets.

According to the above arguments, optical spin-orientation experiments on ferromagnetic systems become possible as soon as spin–orbit coupling is taken into account. In fact, the

symmetry considerations are very much the same as in the non-magnetic case, if the parameter set $\{\vec{n}, \vec{k}, \vec{q}, \vec{\zeta}\}$ is expanded to include the magnetization \vec{M} . Because the initial state in a ferromagnet is already spin polarized, however, the optical orientation process often affects not only the spin polarization of the emitted photoelectrons but also their intensity. This is why optical spin orientation from ferromagnets is often referred to as *magnetic dichroism*. The following sections will concentrate on the mechanisms leading to magnetic dichroism in photoemission under various experimental geometries and conditions.

3. Geometrical considerations: a qualitative approach based on symmetry arguments

Before we turn to the analysis of the band structure and the more elaborate connection of the experimentally observed dichroism with electronic valence states, let us first consider the geometry of the experimental set-up. Similarly to the dipole selection rules discussed in the previous section, which allow us to predict the presence or absence of a certain electronic transition in the photoemission process from symmetry considerations, symmetry arguments can be used to ascertain the presence or absence of dichroism in a certain experimental geometry. This is very useful for the choice of an appropriate experimental geometry for the actual problem, and helps to classify different types of dichroism. The size and spectral shape of the resulting dichroism, however, cannot be accessed by symmetry considerations. It is connected with the electronic properties of the individual system, and contains the desired information about the magnetically split valence band structure. This connection between dichroism and electronic structure will be discussed in section 4.

There are numerous ways to record a dichroism in valence band photoemission. The more interesting ones though will involve some degree of symmetry, be it either to reduce the number of bands involved by means of dipole selection rules, or to map out the band structure along high-symmetry directions in \vec{k} -space. In these cases a simple symmetry consideration involving the crystalline symmetry of the sample can help us to find out easily whether a dichroism can be expected or not.

An experimental geometry is characterized by the arrangement of the unit vectors of the photon and electron momentum, \vec{q} and \vec{k} , respectively, the polarization of the exciting light, \vec{P} , and the direction of the magnetization, \vec{M} . In the case of crystalline samples this arrangement has to be considered with respect to the sample orientation, represented by the surface normal \vec{n} and an azimuthal angle ϕ . The dichroism is then recorded as the difference in photoemission signal between two different sets of \vec{q} , \vec{k} , \vec{P} , and \vec{M} . In general each of these variables may be varied to obtain a change in photoemission. Commonly the term magnetic dichroism is used for the difference between energy distribution curves for opposite magnetization, i.e., spectra acquired for two geometries where \vec{M} is changed to $-\vec{M}$, with the other vectors constant. The term circular dichroism (also magnetic circular dichroism) is usually applied when the helicity of the circularly polarized light is changed from right handed to left handed. Dichroism measurements may also be made by changing \vec{M} by 90° , or by varying the azimuthal direction of the incident light, defined by \vec{q} .

The presence of dichroism means that there exists a difference between the spectra for two different experimental geometries A and B, defined by $\{\vec{q}_A, \vec{k}_A, \vec{P}_A, \vec{M}_A\}$ and $\{\vec{q}_B, \vec{k}_B, \vec{P}_B, \vec{M}_B\}$. The simple symmetry argument for the existence of dichroism is now that there is only dichroism if these two geometries are inequivalent with respect to the symmetry point group of the sample. 'Inequivalent' means that there is no symmetry operation that transforms geometry A into geometry B. In other words, if it is possible to find a symmetry operation of the system which transforms one geometry into the other, then these are equivalent, and no dichroism can exist.

Let us consider a simple example. Figure 6 shows a planar set-up. x , y , and z are sample coordinates, where z points in the direction of the surface normal \vec{n} , and the x - z plane is a mirror plane. The vectors of light incidence \vec{q} and electron emission \vec{k} both lie in that plane. For linear polarization, the light is polarized in the same plane, as indicated in figure 6 by the small double-headed arrow (p polarization). The two configurations differ only in the direction of the magnetization \vec{M} , which in configuration A is in the x -direction, in configuration B in the $-x$ -direction. For the transformation behaviour under symmetry operations we have to keep in mind that \vec{k} , \vec{q} , and the light polarization vector \vec{P} for linear polarization are polar vectors, whereas \vec{M} and \vec{P} for circular polarization are axial vectors. In the example of figure 6, reflection at the x - z plane is a symmetry operation of the system, since the x - z plane is a mirror plane of the crystal. It leaves \vec{k} , \vec{q} , and the light polarization unchanged, since these are polar vectors lying in the mirror plane, but reverses the axial vector \vec{M} . The symmetry operation ‘reflection at the x - z plane’ thus transforms geometry A into geometry B. The consequence is that the two geometries are equivalent for linear polarization, and no dichroism exists.

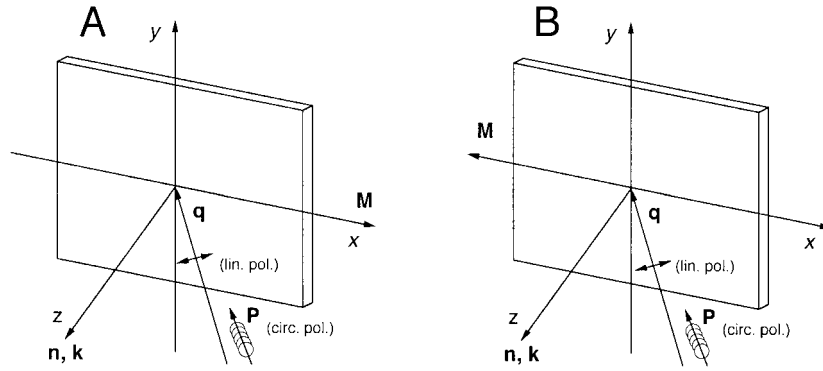


Figure 6. An example of an experimental set-up. Geometries A and B are equivalent in the case of linear polarization, and non-equivalent in the case of circular polarization. Magnetic dichroism in this experiment is thus observed for circular polarization only.

Using circular polarization instead would allow a magnetic dichroism to be observed: in the same geometry as in figure 6 a reflection at the x - z plane would not only transform \vec{M} into $-\vec{M}$, but would also reverse the light helicity (axial vector in the mirror plane). As a matter of fact, there is no symmetry operation which accomplishes a transformation of \vec{M} into $-\vec{M}$ without any other change, so the two geometries A and B are not equivalent for circularly polarized light, opening the way for dichroism. This geometry is very common for the measurement of magnetic circular dichroism. The simultaneous reversal of both the magnetization direction and the light helicity by reflection at the x - z mirror plane implies that reversing both the magnetization direction and helicity in such an experiment creates an equivalent geometry. In this geometry, the dichroism that is obtained by changing only \vec{M} is thus identical to the one obtained by changing only the light helicity.

The behaviour of the dichroism under reversal of magnetization, polarization, or both, can be used to classify different types of dichroism. We will follow the classification and nomenclature of Henk and Johansson [32], and call a dichroism like the present one, where polarization and magnetization reversal compensate for each other, ‘exchange dichroism’. In a more general context it can be represented by averaging the effects of magnetization and polarization reversal:

$$D_{ex} = \frac{1}{2} \left[I(+\vec{P}, +\vec{M}) - I(+\vec{P}, -\vec{M}) - I(-\vec{P}, +\vec{M}) + I(-\vec{P}, -\vec{M}) \right]. \quad (14)$$

The $I(\pm\vec{P}, \pm\vec{M})$ denote the four spectra for the four combinations of light polarization \vec{P} and magnetization \vec{M} . As discussed above, in the present example, the first and fourth, and the second and third terms of equation (14) are equal.

Another commonly employed geometry is shown in figure 7. The light is again incident in the x - z plane. We start with normal emission, i.e., $\vec{k} = \vec{n}$, and the magnetization pointing along y . The x - z and y - z planes will both be mirror planes of the crystal. Let us first consider circular polarization. Reflection at the x - z mirror plane reverses the light helicity only, and leaves the rest of the set-up unchanged. Changing the light helicity therefore does not produce any dichroism. On the other hand, it is not possible to find a symmetry operation which turns \vec{M} into $-\vec{M}$ without any other change. This holds for any light polarization, i.e., also for unpolarized light. Measurements of the so-called linear dichroism are very often performed in this geometry. Reflection at the y - z plane, as illustrated in figure 7, results in a configuration where the magnetization direction and the direction of light incidence with respect to the surface normal are reversed. The dichroism measured by switching the magnetization from up to down can hence be obtained identically by changing the light incidence from the left-hand side to the right-hand side with respect to the surface normal; changing both \vec{M} and \vec{q} results in a null effect.

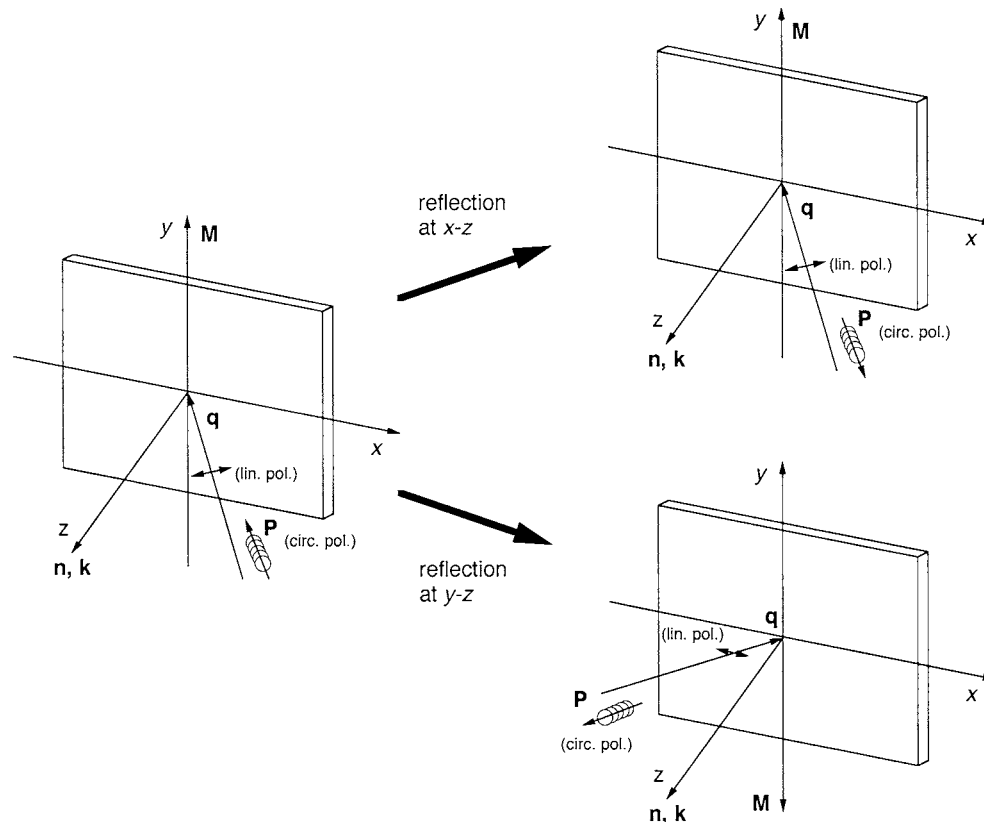


Figure 7. An example of an experimental set-up. Reflection at the x - z plane reverses the helicity in the case of circular polarization. Magnetic dichroism in this experiment can be obtained only by reversing the magnetization \vec{M} . Reflection at the y - z plane shows that reversing the magnetization is equivalent to changing the light incidence direction with respect to the sample surface normal \vec{n} .

This situation resembles the situation of figure 6 with circular polarization. There a change in light polarization, i.e., reversing the light helicity of the circular polarization, yielded the same dichroism as magnetization reversal. Similarly, we can understand the variation of the light incidence direction in figure 7 with respect to \vec{n} , preserving the angle between \vec{q} and \vec{n} and just changing its sign, as ‘switching’ the light polarization in the case of linearly polarized or unpolarized light. In the two cases the results of switching the polarization and the magnetization are the same: switching both leaves zero dichroism. The dichroism in the present example is thus also of the ‘exchange dichroism’ type, and described by equation (14) if we denote the two mirror-symmetric directions of the light incidence by $+\vec{P}$ and $-\vec{P}$.

For experimental geometries with a lower symmetry, the dichroism upon magnetization reversal may differ from the dichroism upon polarization reversal. To sort out the different contributions to the total dichroism in a particular experiment, we define in analogy to equation (14) the dichroism which appears upon reversal of the magnetization only, and is not influenced by the light polarization. An example of this situation is represented in figure 7 (with circular polarization). Following reference [32], we call this dichroism D_{mag} :

$$D_{mag} = \frac{1}{2} \left[I(+\vec{P}, +\vec{M}) - I(+\vec{P}, -\vec{M}) + I(-\vec{P}, +\vec{M}) - I(-\vec{P}, -\vec{M}) \right]. \quad (15)$$

Here any change in the spectra generated by changing the polarization \vec{P} is averaged out. A geometry where a ‘pure’ exchange-type dichroism is encountered (cf. figure 6 with circular polarization) has $D_{mag} = 0$.

A third class of dichroism can be defined by

$$D_{pol} = \frac{1}{2} \left[I(+\vec{P}, +\vec{M}) + I(+\vec{P}, -\vec{M}) - I(-\vec{P}, +\vec{M}) - I(-\vec{P}, -\vec{M}) \right]. \quad (16)$$

In this equation all effects induced by variation of \vec{M} cancel out, leaving the dichroism which occurs solely due to a variation of the light polarization \vec{P} . An example is a set-up like that in figure 6 with linear polarization. As outlined before, reversing the magnetization results in an equivalent geometry, so no dichroism occurs. ‘Reversing’ the polarization by turning the azimuthal direction of the light incidence by 180° , on the other hand, results in an equivalent geometry only if the y - z plane is a mirror plane, and the emission is along the surface normal. Only in that case does a reflection at the y - z plane transform the set-up with \vec{q} on one side into an identical set-up, except for \vec{q} being on the other side. In all other cases, the two geometries are inequivalent, leading to the possible presence of dichroism.

It should be noted at this point that the presence of \vec{M} is not necessary for observing D_{pol} . In the literature, D_{pol} is sometimes also called spin-orbit dichroism. Considering a situation like the one shown in figure 7, but without \vec{M} , there is still no symmetry operation for off-normal emission which would turn \vec{q} to the other side. In this geometry a dichroism is measured also for non-magnetic samples, which has been termed linear dichroism in angular distribution. This example highlights the close relationship of D_{pol} to dichroism in photoemission from non-magnetic solids.

In a general experimental set-up of a lower symmetry, all three types of dichroism, D_{ex} , D_{mag} , and D_{pol} , may be non-zero. The above equations (14)–(16) may then be used to classify the different contributions to the observed ‘total’ dichroism, represented by the set of four (in that case inequivalent) spectra $I(+\vec{P}, +\vec{M})$, $I(+\vec{P}, -\vec{M})$, $I(-\vec{P}, +\vec{M})$, and $I(-\vec{P}, -\vec{M})$. D_{ex} is thereby related to magnetic circular dichroism, D_{pol} to magnetic unpolarized dichroism, and D_{mag} to non-magnetic dichroism.

An example in which all three types of dichroism are present is given in figure 8. Here we consider normal emission, circular polarization, and a fourfold crystal symmetry, i.e., both the x - z and y - z planes are mirror planes. The magnetization is along the x -axis. This set-up is a

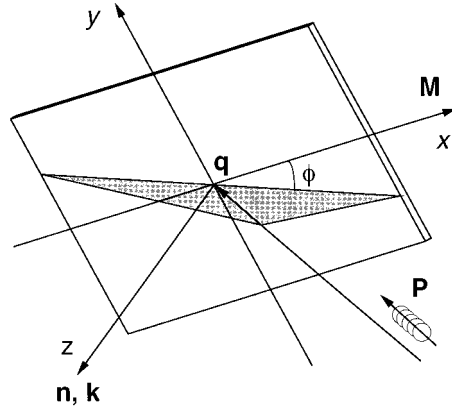


Figure 8. An example of an experimental set-up of lower symmetry. The sample azimuth direction is turned by an angle ϕ with respect to the reaction plane defined by \vec{q} and \vec{k} . Reversing the light polarization \vec{P} or the magnetization \vec{M} results in a different dichroism in this experiment.

generalization of the situation of figures 6 and 7, in that the azimuthal angle ϕ is introduced, and the reaction plane defined by incident photon and emitted electron is in general no longer a mirror plane of the solid. For $\phi = 0$ a situation similar to that of figure 6 is encountered, and only D_{ex} is non-zero, as discussed before. $\phi = 90^\circ$ represents the situation of figure 7 for circular polarization. Here only D_{mag} is non-zero, since a reversal of the helicity results in an equivalent geometry, and hence $I(+\vec{P}, +\vec{M}) = I(-\vec{P}, +\vec{M})$ and $I(+\vec{P}, -\vec{M}) = I(-\vec{P}, -\vec{M})$. For oblique azimuthal angles $0 < \phi < 90^\circ$, all three, D_{ex} , D_{mag} , and D_{pol} , are non-zero. No symmetry operation can then be found which would convert a magnetization reversal into a helicity reversal, or transform this geometry into another, equivalent one, with opposite magnetization or light polarization.

Henk and Johansson introduced the term ‘double dichroism’ for a situation in which two or three of the different types of dichroism, D_{ex} , D_{mag} , and D_{pol} , are non-zero [32]. ‘Double’ thereby indicates that unlike the case for the ‘normal’ dichroism, where we are dealing with two different spectra, in the case of double dichroism there are four inequivalent spectra for the four possible arrangements which are obtained by reversing both the light polarization and the magnetization direction. Depending upon the problem in the example of figure 8, ϕ may be set to a particular value in order to increase the sensitivity to one of the different types of dichroism.

In the next section we will discuss a D_{ex} that is caused by differences in dipole transition probability for electronic states whose degeneracy is lifted by the simultaneous presence of spin–orbit and exchange interaction. In section 4.2, D_{mag} will be shown to be an interference effect, resulting from the interference between different matrix elements. In section 4.4 we will see that D_{pol} can be interpreted as a transmission effect, which influences the off-normal emission of photoelectrons which are spin polarized due to the presence of spin–orbit coupling.

4. Selected experimental results

Before we can analyse the experimental results, it is necessary to study the details of the relativistic band structure of a ferromagnet. We start the discussion of experimentally observed magnetic dichroism with examples for perpendicularly magnetized samples. If the magnetization is perpendicular to the sample surface, the overall symmetry of the system is

higher than for in-plane magnetization, because the rotational symmetry around the surface normal is preserved. In that case the relativistic band structure of the magnetic sample can be deduced from the non-magnetic band structure in a more inductive way. We will discuss two selected examples from the literature, which cover the cases of a fourfold- and a threefold-symmetric sample. In both examples the dichroism is purely D_{ex} -type. After that we turn to the case of in-plane magnetization, where a D_{mag} -type dichroism will be analysed. The section will be concluded by examples involving a set-up of lower symmetry, where the contribution of D_{pol} is discussed.

4.1. Normal emission, circular polarization, perpendicular magnetization

4.1.1. Fourfold symmetry: Ni/Cu(100). Ni films grow pseudomorphically on the (100) surface of Cu for thicknesses below ≈ 15 atomic monolayers (ML) [33–39]. The fact that the bulk lattice constant of Ni (3.56 Å) is smaller than that of Cu (3.61 Å) is reflected in a tetragonal compression of the pseudomorphic Ni films along the film normal [37, 38]. Magnetoelastic effects connected with this compression are held to be responsible for the perpendicular easy axis of magnetization of Ni/Cu(100) for an extended range of film thicknesses [33, 34, 40]. The tetragonal distortion does not, however, lower the symmetry of the system with respect to a pure fcc structure, since the presence of the surface already breaks the symmetry in the direction of the sample normal. The fourfold symmetry of that system is thus still described by the symmetry group C_{4v} . Its five classes of symmetry operations can be represented by the five irreducible representations Δ^1 , Δ^1 , Δ^2 , Δ^2 , and Δ^5 (see the first column in table 1).

Before we move to the relativistic electronic structure of Ni, it is useful to inspect the corresponding non-magnetic case. The non-magnetic metal closest to Ni in the periodic table is Cu itself. The spin-orbit coupling in Cu is weaker than that in Ag, resulting in a smaller splitting of the Δ^5 bands. From experimental data it is known that the spin-orbit splitting of the Δ^5 states is of the order of $\Delta_{soc} \approx 100$ meV [41]. If we assume the same splitting to hold for ‘non-magnetic’ (NM) Ni, we can construct the hypothetical band structure displayed in figure 9. It reflects the situation along the Δ axis of a paramagnetic fcc 3d transition metal. For reasons of clarity, we have drawn the bands before and after the spin-orbit-induced hybridization. It is instructive to compare these graphs with the bands along the Δ axis in Ag (figure 3). The difference in magnitude of the band splitting causes a distinct variation in the shape of the bands when going from Ag to NM Ni, specifically in the bottommost Δ_6 band. A part of this variation is also caused by the fact that the upper Δ^1 band intersects the Δ^5 states in NM Ni twice, whereas it only touches the respective band in Ag. The consequence is that there is a strong Δ^1 – Δ^5 hybridization already in the non-magnetic case.

Application of non-relativistic dipole selection rules, which can be found for example in reference [42], results in transitions $\Delta^5 \rightarrow \Delta^1$ for normal incidence, and $\Delta^1 \rightarrow \Delta^1$ for the case of grazing incidence. Both transitions are allowed if the polarization vector of the exciting light contains projections of both extremes, as is the case for oblique incidence. In the following we will restrict consideration to normal incidence, and emission from $\Delta^5 \rightarrow \Delta^1$ transitions only; this is the reason that in figure 9 (and in the following figures) initial-state bands with Δ^5 symmetry are represented by thicker lines compared to those for bands with other symmetries.

For didactic reasons we will now include the ferromagnetic exchange interaction again in two steps, as we did before when we introduced the spin-orbit interaction. After these two steps, we will end up with the ferromagnetic relativistic band structure, which is necessary for the interpretation of the magnetic dichroism. The two steps are illustrated in figure 10. In the first step, as before, band mixing by hybridization is neglected. We first construct the band

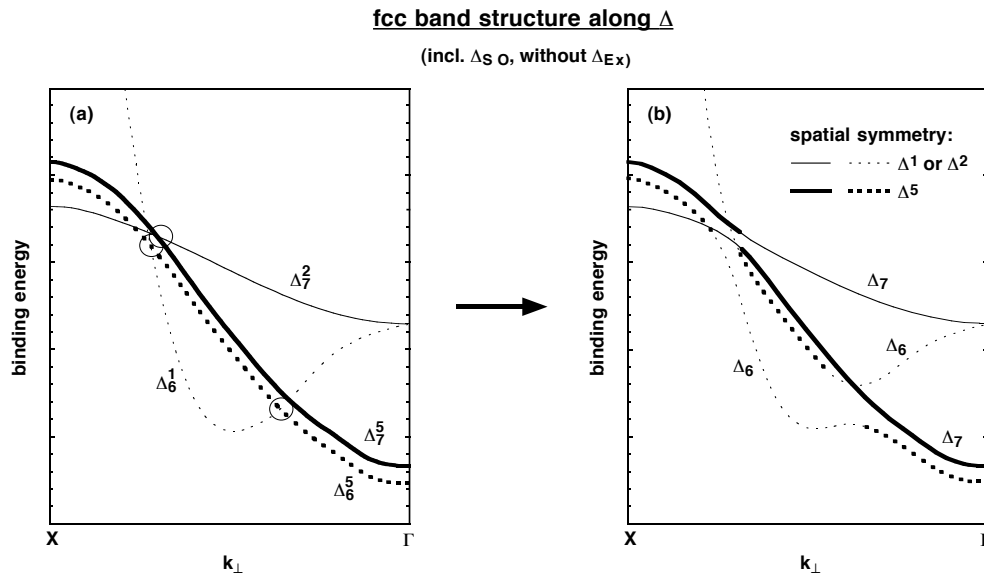


Figure 9. Construction of the relativistic band structure for non-magnetic Ni along the Δ axis. (a) The intermediate step without consideration of spin-orbit-induced hybridizations. All bands can be labelled according to their non-relativistic spatial symmetry (superscript), and the relativistic double-group representation (subscript). (b) The relativistic band structure, obtained from (a) by lifting forbidden degeneracies marked by circles. The spatial symmetry is no longer conserved within the bands. The predominant part of the spatial symmetry is indicated by the thickness of the lines.

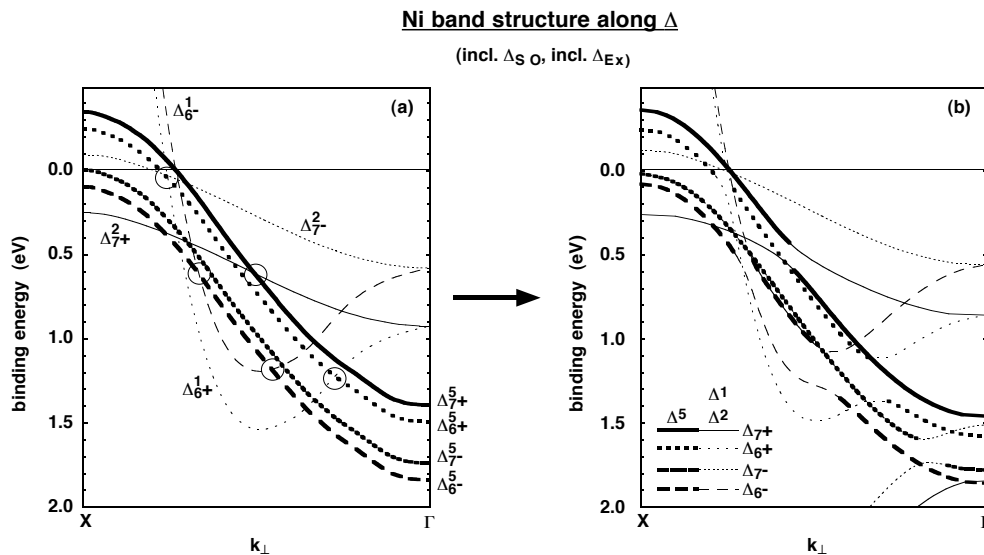


Figure 10. (a) The intermediate step for the construction of the relativistic band structure of ferromagnetic Ni along the Δ axis. All bands can be labelled according to their non-relativistic spatial symmetry, relativistic double-group symmetry, and time-reversal symmetry (+ or -). (b) The relativistic band structure of Ni, calculated for the tetragonally distorted structure of a 15 ML Ni film on Cu(100), and perpendicular magnetization (from reference [37]). It shows the lifting of forbidden degeneracies, marked by circles in (a), by interband hybridizations. Bands with predominant Δ^5 spatial symmetry are indicated by thick lines.

structure regardless of whether bands are allowed to cross each other or not. The left-hand side of figure 10 shows this intermediate result. It is obtained by simply splitting the band structure of figure 9(a) into two subsets of bands, and shifting them apart by the exchange energy Δ_{ex} . This would correspond to the Stoner picture of ferromagnetism, where all bands exhibit a constant exchange splitting. The bands which have been shifted upwards in energy would represent pure minority-spin states, the bands shifted downwards pure majority-spin states.

For shifting the bands and positioning them into an energy scale with respect to the Fermi level (0 eV), the band structure of Ni was used as a template. The average exchange splitting in Ni is only about 0.3 eV, which is a lot smaller than the bandwidth of the 3d bands. This is the reason for the complicated-looking band structure of figure 10(a). Up to here, not only the electron spin, but also the spatial symmetry is well defined for each band, like it was during the construction of the non-magnetic case in figure 9(a). Again, the mixing of the spatial symmetry within the bands, and now also of the spin, follows from hybridization due to the lifting of forbidden degeneracies. This is the second step, which we will consider now.

To decide which band crossings are allowed and which are not, we need to know the symmetry representation of the bands. As mentioned at the beginning of this section, we are restricting consideration here to a magnetization direction perpendicular to the surface normal. This results in a higher symmetry of the magnetic system than an in-plane magnetization. The presence of the magnetization breaks the time-reversal symmetry. Since the electron spin is no longer a good quantum number in the presence of spin-orbit coupling, and thus cannot be used to label the bands in the ferromagnetic case, we classify them according to the symmetry behaviour under time reversal, and append a + or – sign to the double-group symmetry of the non-magnetic case. In doing this we follow the nomenclature of reference [44], which is the most convenient one for the interpretation of magnetic dichroism. Four irreducible representations of the magnetic double group, Δ_{7+} , Δ_{6+} , Δ_{7-} , and Δ_{6-} , are the result. For bands with pure spatial symmetry, a direct relation between the electron spin and the time-reversal symmetry can be given:

$$\begin{aligned}
 \Delta_{6+}^1 &\longrightarrow |\uparrow\rangle & \Delta_{6-}^1 &\longrightarrow |\downarrow\rangle \\
 \Delta_{7+}^2 &\longrightarrow |\uparrow\rangle & \Delta_{7-}^2 &\longrightarrow |\downarrow\rangle \\
 \Delta_{6+}^5 &\longrightarrow |\downarrow\rangle & \Delta_{6-}^5 &\longrightarrow |\uparrow\rangle \\
 \Delta_{7+}^5 &\longrightarrow |\downarrow\rangle & \Delta_{7-}^5 &\longrightarrow |\uparrow\rangle.
 \end{aligned}
 \tag{17}$$

We have to note that this relation is not unique, because it depends on the definition of + and – time-reversal symmetry. Here we will adopt the definition of Scheunemann *et al* [44], from which the correlations follow as listed above. In the hypothetical case of figure 10(a) there is no mixing of spatial symmetries, and the correlations between spin and time reversal are fully valid. Each band can thus be labelled unambiguously by the irreducible representation of the double group in the magnetic case, and its spatial symmetry. According to these labels, it is now possible to check for forbidden crossings. They occur whenever bands with the same (magnetic) double-group symmetry are crossing each other. For the bands depicted in figure 10(a) this is the case five times, as marked by the small circles. Close to the Fermi energy, for example, a steep Δ_{6+}^1 band is crossing the Δ_{6-}^5 band, and so on. These forbidden degeneracies are lifted in figure 10(b). It shows the result of a band-structure calculation for a semi-infinite Ni crystal with the structural parameters of a 15 ML Ni/Cu(001) film from reference [37]. In addition to the five degeneracies marked in figure 10(a), there is also a crossing of a Δ_{7-} band in the lower right-hand corner of figure 10(b), which has not been considered in the previous figures. By following the bold lines representing Δ^5

spatial symmetry, it is easily recognized that at the hybridization points the spatial symmetry is exchanged between different bands. In the magnetic case, the spin is also changing within the same band: from equation (17) it follows that a hybridization between a (majority) Δ_{6+}^1 band and a (minority) Δ_{6+}^5 band, such as occurs twice in figure 10, not only changes the spatial symmetry of the participating bands between Δ^1 and Δ^5 , but also changes the spin between majority and minority.

To understand the origin of the magnetic dichroism in our example, we recall the relativistic selection rules from table 4 (cf. reference [14]). We simply transfer these selection rules to the magnetic case, where we correlate the electron spin with the time-reversal symmetry according to equation (17). We have to take it into consideration that now the bands are no longer occupied by electrons of both spin directions, as in the paramagnetic case. It follows that only transitions from Δ_{6+}^5 and Δ_{7-}^5 bands are allowed for right circularly polarized light (Δ_{6-}^5 and Δ_{7+}^5 for left circularly polarized light), because of the spin sensitivity of the transitions. Changing the light helicity thus results in emission from different, non-degenerate bands, which leads to different photoemission spectra for the two helicities. This is the origin of the magnetic circular dichroism.

This result is corroborated by the analytic considerations of Henk *et al* [45]. The present geometry (normal light incidence, circular polarization, and normal electron emission) is depicted in figure 11. For this geometry, the analytic result from reference [45] reads

$$\begin{aligned} I(\uparrow\uparrow) &= 2(|M_6^{+-}|^2 + |M_7^{-+}|^2) \\ I(\uparrow\downarrow) &= 2(|M_6^{-+}|^2 + |M_7^{+-}|^2). \end{aligned} \quad (18)$$

$I(\uparrow\uparrow)$ and $I(\uparrow\downarrow)$ are the photoemission intensities for parallel and antiparallel alignment of the light helicity and sample magnetization, respectively, as defined in figure 11. As discussed in section 3, in this geometry, reversal of the light helicity direction and reversal of the magnetization direction are equivalent, so the spectra $I(\uparrow\uparrow) = I(\downarrow\downarrow)$ and $I(\uparrow\downarrow) = I(\downarrow\uparrow)$ have to be identical. In this notation, M_6^{+-} stands for the matrix element for transition from a Δ_{6-}^5 initial state to a Δ_{6+}^1 final state, M_7^{-+} for the matrix element for transition from a Δ_{7+}^5 initial state to a Δ_{6-}^1 final state, etc. The exchange splitting in the final-state bands between Δ_{6+}^1 and Δ_{6-}^1 is very small, so the main effect arises in fact from the selection of different initial-state bands for the two light helicities. The squares of the transition matrix elements in equation (18) indicate that $I(\uparrow\uparrow)$ and $I(\uparrow\downarrow)$ can be interpreted as composed by the incoherent superposition of intensities of two different transitions, which we had already intuitively become aware of by using the selection rules of table 4 in the magnetic case.

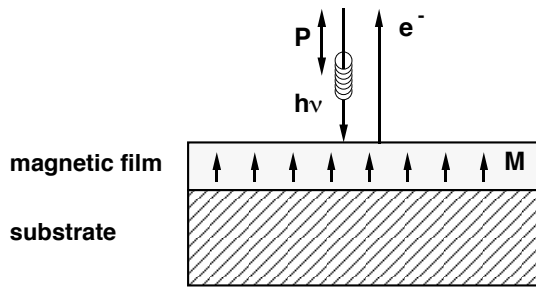


Figure 11. The totally symmetric experimental geometry. The circularly polarized light ($h\nu$) is incident perpendicularly to the surface plane. The magnetic film is perpendicularly magnetized; the light helicity \vec{P} is either parallel or antiparallel to the magnetization direction \vec{M} . Electrons e^- are detected in normal emission.

The situation is illustrated in figure 12. It shows in the bottom panel schematically the energetic positions of the four bands involved, Δ_{6-}^5 , Δ_{7-}^5 , Δ_{6+}^5 , and Δ_{7+}^5 . Arrows indicate the interplay of Δ_{so} and Δ_{ex} in the energetic separation of these bands. In the centre panel, schematic intensity distribution curves $I(\uparrow\uparrow)$ (solid line) and $I(\uparrow\downarrow)$ (dotted line) for the two cases are reproduced. The resulting dichroism, i.e., the difference between the two spectra, is shown in the top panel. It exhibits a characteristic positive/negative/positive overall shape, with an indentation in the middle. The positive/negative/positive shape is a consequence of equation (18), which describes the excitation of photoelectrons from the two (energetically) outer bands in the case of parallel alignment of \vec{P} and \vec{M} , and from the inner bands in the case of antiparallel alignment.

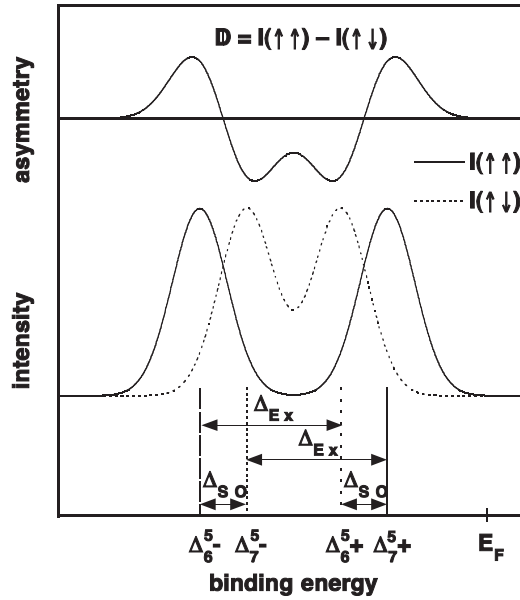


Figure 12. Bottom: a schematic representation of the four bands of Δ_{6-}^5 , Δ_{7-}^5 , Δ_{6+}^5 , and Δ_{7+}^5 symmetry contributing to the spectra in the totally symmetric experimental geometry. The arrows indicate the splitting due to spin-orbit (Δ_{so}) and exchange interaction (Δ_{ex}). Centre: schematic intensity distribution curves for parallel ($I(\uparrow\uparrow)$, solid line) and antiparallel alignment ($I(\uparrow\downarrow)$, dotted line) of the photon spin and magnetization directions. Top: the difference D of the spectra of the centre panel. (From reference [46].)

Figure 13 shows the result of a photoemission calculation from reference [37] for a photon energy of $h\nu = 21.1$ eV. In the bottom panel (a) the calculated Ni band structure from figure 10(b) is reproduced, this time without highlighting the bands with Δ^5 symmetry. The dash-dotted line represents the final-state bands, shifted downwards in energy by $h\nu$. The exchange splitting of the final-state bands is not visible on the scale of figure 13. The crossings of this line with bands with Δ^5 symmetry give the positions in k -space where transitions for that photon energy occur. These crossings are marked by vertical lines. They connect the band structure of panel (a) with the result of a spin-resolved photoemission calculation, shown in panel (b). Each of the four bands with Δ^5 spatial symmetry gives rise to a peak in one of the four partial spectra of figure 13(b). In addition, in the Δ_{7+} spectra, a peak at 0.45 eV binding energy is observed. This is a consequence of hybridization between Δ_{7+}^5 and Δ_{7+}^2 states, as discussed before. It leads to the two Δ_{7+} bands in the hybridization region simultaneously showing Δ^5 spatial symmetry; this region is about at the position where the transitions at

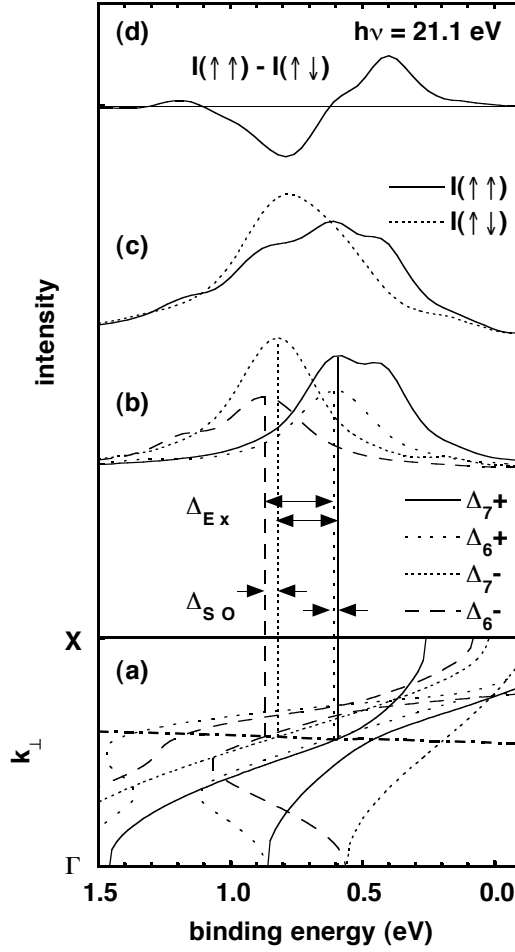


Figure 13. A theoretical illustration of the origin of the observed MCDAD. (a) The calculated fully relativistic Ni band structure from figure 10(b) for perpendicular magnetization. The bands are distinguished by their relativistic double-group symmetries Δ_{7+} , Δ_{6+} , Δ_{7-} , and Δ_{6-} . The final-state band, shifted down by 21.1 eV, is shown as a dash-dotted line. The vertical lines mark crossing points of the shifted final-state band with four initial bands of predominantly Δ^5 spatial symmetry. The influence of spin-orbit (Δ_{so}) and exchange interaction (Δ_{ex}) on the energetic separation of these bands is indicated by arrows. (b) Spin-resolved photoemission spectra for 21.1 eV photon energy, calculated with the same parameters as the band structure of panel (a). The spectra are labelled in correspondence with the underlying initial-state bands. (c) Calculated photoemission intensity spectra for parallel ($I(\uparrow\uparrow)$, solid line) and antiparallel ($I(\uparrow\downarrow)$, dotted line) alignment of the light helicity and magnetization directions. The spectra are related to the spin-resolved spectra of (b) by $I(\uparrow\uparrow) = I(\Delta_{7+}) + I(\Delta_{6-})$ and $I(\uparrow\downarrow) = I(\Delta_{7-}) + I(\Delta_{6+})$. (d) The difference of the two curves of (c), showing the dichroism. (From reference [37].)

$h\nu = 21.1$ eV take place. Similarly, a bump in the Δ_{6-} spectra at 1.2 eV is correlated with hybridization between Δ_{6-}^5 and Δ_{6-}^1 states at around 1 eV binding energy.

In a spin-integrating photoemission experiment using circularly polarized excitation, spectra like the ones shown in the next panel, figure 13(c), would be observed. $I(\uparrow\uparrow)$ and $I(\uparrow\downarrow)$ denote again spectra for parallel and antiparallel alignment of the light helicity and magnetization, respectively. The theoretical spectra of figure 13(c) were obtained by summing

pairs of spectra of figure 13(b), using equation (18): the sum of the spectra denoted by Δ_{7+} and Δ_{6-} gives $I(\uparrow\uparrow)$; the sum of the spectra denoted by Δ_{7-} and Δ_{6+} gives $I(\uparrow\downarrow)$.

The top panel (figure 13(d)) finally shows the resulting theoretical dichroism $I(\uparrow\uparrow) - I(\uparrow\downarrow)$. In contrast to the simple schematic explanation of figure 12, the positive/negative/positive shape is not very pronounced at this photon energy, because the positive peak on the higher-binding-energy side is very small. The reason for that is found in the details of the band structure. At 21.1 eV photon energy the bands are probed at a position where the contribution from the lower-lying band at 1.2 eV binding energy due to $\Delta_{6-}^5/\Delta_{6-}^1$ hybridization is rather small, and the higher-lying Δ_{6-} band is shifted upwards in energy with the result that it is nearly degenerate with the Δ_{7-} band. This is also clearly seen by comparing figures 10(a) and 10(b). This small energetic separation between the Δ_{6-} and Δ_{7-} contributions leads to nearly coinciding peaks in $I(\uparrow\uparrow)$ and $I(\uparrow\downarrow)$, and thus to the reduction of the positive feature in the difference spectra on the high-binding-energy side.

An experimental set of spectra demonstrating the selected-transition origin of the magnetic dichroism in this geometry is shown in figure 14. Figure 14(a) shows spin-resolved photoemission spectra taken with 15.3 eV photon energy for the four combinations of electron spin (majority or minority), and photon helicity (parallel or antiparallel) [47]. The sequence of four different spectra with peaks of increasing binding energy, as expected from the above considerations, can be clearly distinguished. The correlation with the initial-state

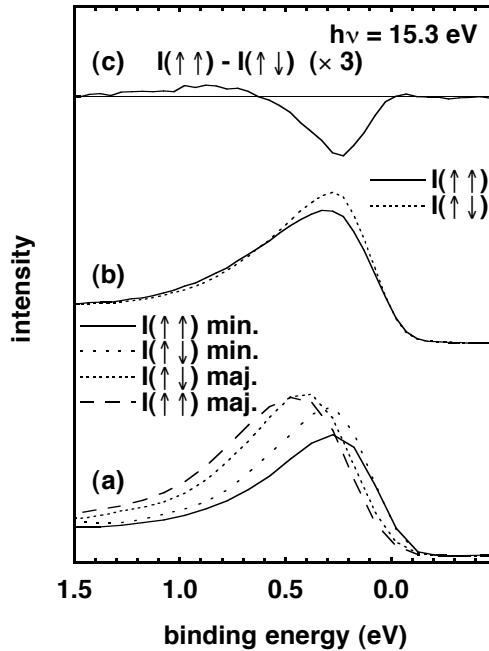


Figure 14. An experimental illustration of the origin of the observed MCDAD. (a) Experimental spin-resolved photoemission spectra for 15.3 eV photon energy. The spectra are labelled according to the four inequivalent combinations of electron spin (majority or minority), and photon helicity (parallel or antiparallel to the magnetization direction) [47]. To facilitate the correlation with the four different double-group symmetries, the line type of the spectra corresponds to the set of theoretical spectra of figure 13(b). (b) Experimental intensity spectra for parallel ($I(\uparrow\uparrow)$, solid line) and antiparallel alignment ($I(\uparrow\downarrow)$, dotted line) of the photon spin and magnetization directions [37]. (c) The difference of the two spectra of (b), scaled by a factor of 3, showing the dichroism.

bands according to the four different magnetic double-group representations, as explained in figures 12 and 13, is as follows: since the Δ^5 part of a Δ_{7+} band has minority spin (cf. equation (17)), and states can be observed only with light which is circularly polarized parallel to the magnetization direction (cf. equation (18)), the minority $I(\uparrow\uparrow)$ spectrum of figure 14(a) represents Δ_{7+} bands. Similarly, the majority $I(\uparrow\uparrow)$ spectrum represents Δ_{6-} , the minority $I(\uparrow\downarrow)$ spectrum Δ_{6+} , and the majority $I(\uparrow\downarrow)$ spectrum Δ_{7-} bands.

Figure 14(b) shows experimental intensity spectra for parallel (solid line) and antiparallel (dotted line) alignment of the light helicity and magnetization. These spectra (from reference [37]) correspond to the pairwise sums of the spin-resolved spectra of panel (a). They exhibit a sizable dichroism at the peak maximum, and also in the higher-binding-energy shoulder. The overall spectroscopic information in these spectra is somewhat less than that in the set of spin-resolved spectra of panel (a); it has to be kept in mind, however, that the acquisition time for a comparable statistics is two or three orders of magnitude shorter if no spin detection is needed. Exploiting the effect of magnetic dichroism enables the experimenter to take a complete series of intensity spectra like the ones shown in figure 14(b), mapping out the electronic states in k -space, in less time than would be needed to take one single set of spin-resolved spectra like the one shown in figure 14(a).

The top panel of figure 14 shows the resulting dichroism $I(\uparrow\uparrow) - I(\uparrow\downarrow)$ obtained from the two spectra of panel (b). It shows a pronounced negative peak at 0.25 eV binding energy, and a smaller positive peak around 0.9 eV. These two peaks are part of the expected positive/negative/positive series (cf. figure 12). The first positive peak in the experimental spectra (towards low binding energies) does not show at that photon energy because it is cut off by the Fermi edge. This is corroborated by the height of the spin-resolved spectra of panel (a). The peak in the minority $I(\uparrow\uparrow)$ spectrum is less intense than the peaks in the other three spectra, which is an indication that the Δ_{7+}^5 band is about at the Fermi energy, and part of its intensity is cut off, which otherwise would have caused a positive peak in the difference spectra on the lower-binding-energy side. The negative peak is connected with the summation of the inner two spectra of figure 14(a). For a symmetric arrangement of the four contributing bands and peak widths, this negative peak should follow the dispersion of the centre of the four bands with Δ^5 symmetry.

A series of experimental intensity spectra for different photon energies from 11.1 up to 27.4 eV was published in reference [37], and is reproduced on the left-hand side of figure 15. As in figures 13 and 14, spectra for parallel and antiparallel alignment of the light helicity and magnetization directions are represented by solid and dotted lines, respectively. The spectra for 15.3 eV photon energy are the ones already shown in figure 14(b). The vertical lines mark peak positions where a Δ_{7+} hybridization can be identified, which will be discussed later.

The right-hand side displays the corresponding calculated photoemission spectra. Here, the spectra for 21.2 eV photon energy have already been reproduced in figure 13(c). Good qualitative agreement between experiment and theory can already be seen at first sight. The spectra for 11.1 eV photon energy display relatively sharp peaks just below the Fermi energy. With increasing photon energy a dispersion towards higher binding energies, and a broadening of the peaks are observed. The higher intensity in the peak maximum of the dotted curves in the spectra from $h\nu = 11.1$ up to 21.1 eV is reproduced well in the theory. Sharp structures are better resolved in the theoretical curves. For the comparison of theory and experiment, however, it has to be noted that the calculations have deliberately been performed with an unrealistically low value of the imaginary part of the optical potential, in order to facilitate the connection with the band structure [37]. Furthermore, the effects of finite energetic and angular resolution, finite temperature, inelastic background, and possible morphological film imperfections were not considered in the calculation. The spectra for $h\nu = 21.1$ eV have

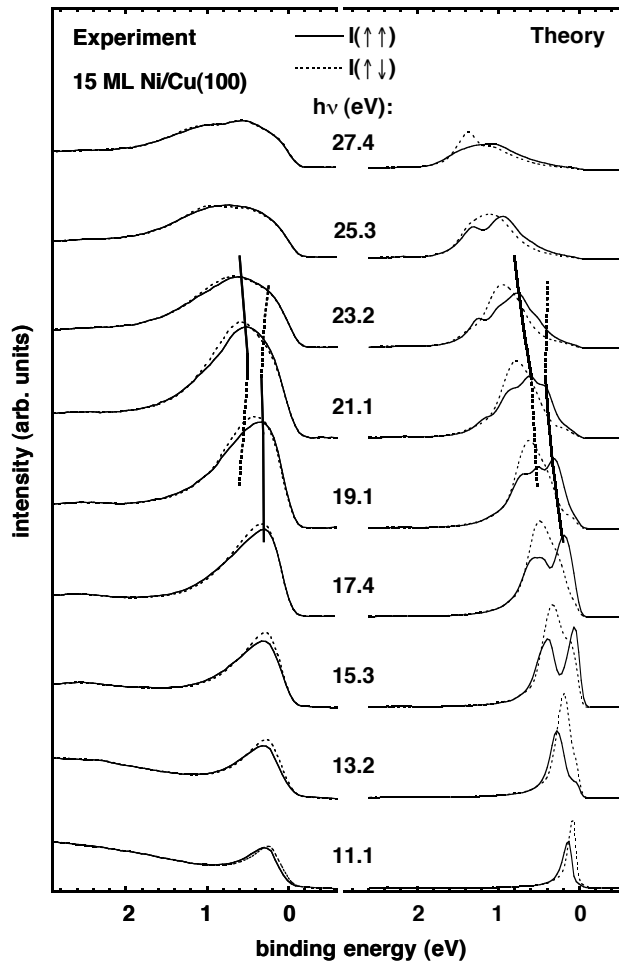


Figure 15. Series of partial intensity spectra for different photon energies $h\nu$, as indicated. Shown are spectra for parallel ($I(\uparrow\uparrow)$, solid line) and antiparallel alignment ($I(\uparrow\downarrow)$, dotted line) of the photon spin and magnetization directions. Left: experimental spectra; right: theoretical spectra. The vertical lines indicate the occurrence of a hybridization region as explained in the text. (From reference [37].)

been recalculated with more realistic parameters by Henk and Johansson in reference [32], and are reproduced at the bottom of figure 27(e)—see later. The overall agreement with the experimental results is much improved, but the identification of the detailed structure within a spectrum is more difficult than for the sharper structures of figure 15.

The dichroism of the spectra of figure 15 is shown in figure 16. In contrast to the previous figures, where the dichroism was displayed as the difference $I(\uparrow\uparrow) - I(\uparrow\downarrow)$ of the spectra for opposite light helicity or sample magnetization, here the normalized asymmetry A is displayed. The asymmetry is defined as $A = [I(\uparrow\uparrow) - I(\uparrow\downarrow)]/[I(\uparrow\uparrow) + I(\uparrow\downarrow)]$. Again, experimental results are depicted on the left-hand side, theoretical results on the right-hand side. To facilitate comparison with the experimental data, the theoretical asymmetry curves have been scaled down by a factor of 0.2. The reasons for this substantial size difference between experiment and theory lie in the details of the calculation, as already mentioned above. Apart from the

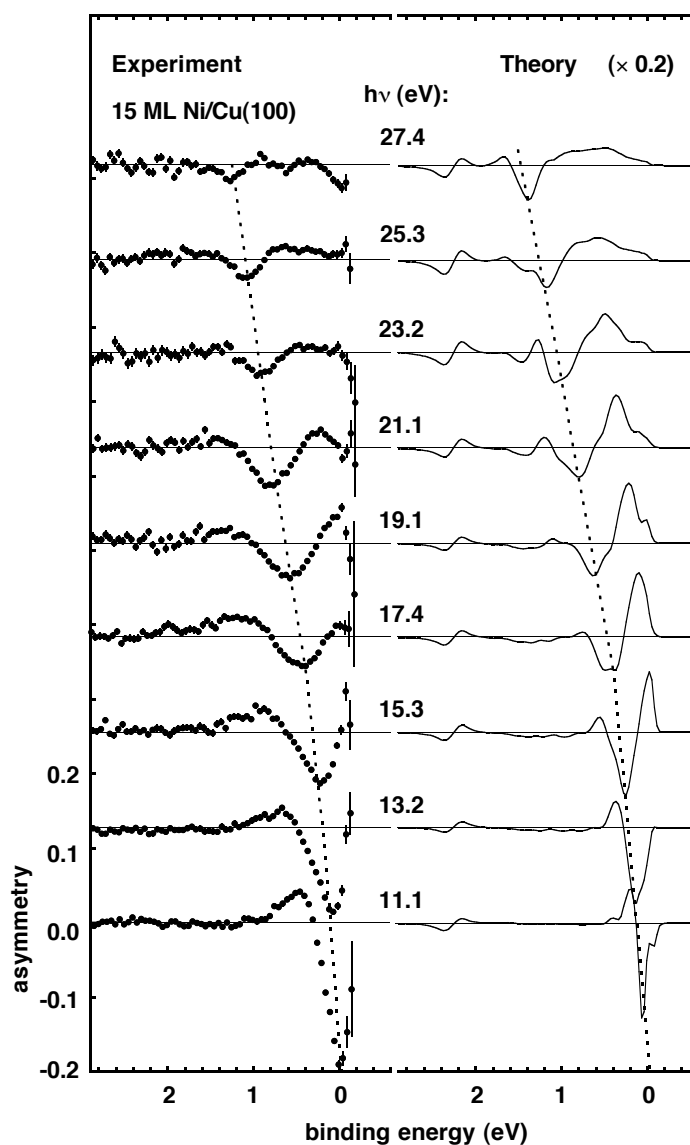


Figure 16. Series of asymmetry spectra for different photon energies $h\nu$, calculated from the corresponding spectra of figure 15 as $[I(\uparrow\uparrow) - I(\uparrow\downarrow)]/[I(\uparrow\uparrow) + I(\uparrow\downarrow)]$. Left: experimental asymmetries; right: theoretical asymmetries, scaled by a factor of 0.2. The dotted lines mark the dispersion of the prominent negative peak. (From reference [37].)

different scale, the agreement between experiment and theory in figure 16 is rather good. At all photon energies there is one pronounced negative feature which disperses towards higher binding energies with increasing photon energy. The dotted lines in figure 16 indicate this dispersion. As mentioned before, in the ideal case they reflect the dispersion of the centre of the bands with Δ^5 spatial symmetry, disregarding possible interband hybridizations. Its experimental observation allows an estimation of the band dispersion, which would be very difficult from intensity spectra alone (figure 15).

In figure 17 the theoretical band structure from reference [37] is reproduced; it was calculated using the same parameters as the theoretical spectra in figures 15 and 16, and had been introduced already in figures 10(b) and 13(a). In figure 17, however, only those parts of the bands which have Δ^5 spatial symmetry to a measurable extent are shown. It is very clearly seen how hybridization due to lifted degeneracies affects the energetic positions of the experimentally observable bands (for the hypothetical case of no hybridization, compare figure 10(a)). To establish the correlation between the band structure and the photoemission spectra more easily, nine sections of the calculated final-state band, shifted down by the nine photon energies used in the experiment (cf. figures 15 and 16), are depicted in figure 17 as thin solid lines. The comparison, similar to that in figure 13, of the calculated photoemission spectra (right-hand side of figure 15) and the band structure (figure 17) for all nine photon energies shows the validity of the interpretation of the spectra in terms of direct interband transitions [37]. All features of the calculated spectra can be correlated with transitions from the initial-state bands shown in figure 17. As an example, let us consider the hybridization of bands with Δ_{7+} symmetry (solid lines in figure 17). They exhibit a hybridization gap around $k_{\perp} = 0.55\pi/a$ at binding energies between 0.4 and 0.6 eV. This hybridization should occur in the photoemission spectra at 19.1 and 21.1 eV photon energy. In figure 13 it was already shown how this Δ_{7+} hybridization affects the calculated spectra. The vertical lines in figure 15

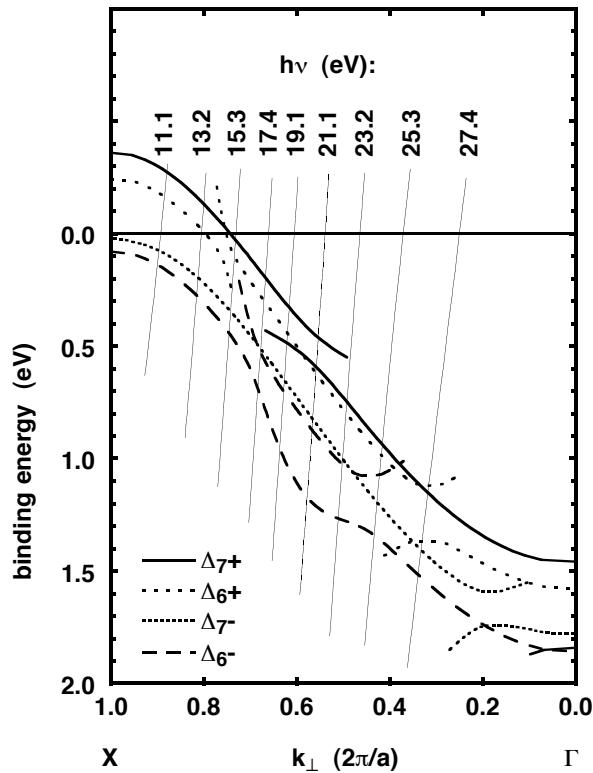


Figure 17. Calculated valence band structure of Ni, as in figures 10(b) and 13(a) [37], showing only the part of the band structure with a measurable proportion of Δ^5 spatial symmetry. Bands of different double-group symmetry are distinguished as labelled in the figure. The thin solid lines are sections of the final-state band, shifted down by the nine different photon energies used in figures 15 and 16, indicated at the respective lines.

indicate this hybridization region. They mark the corresponding peaks in the spectra (solid lines), and fade out into dotted lines where the proportion of Δ^5 spatial symmetry approaches zero. In the calculated spectra (right-hand side of figure 15), the two hybridizing bands can be distinguished as separate peaks, thanks to the unrealistically low imaginary potential used for the calculation. It is clearly seen how the hybridization leads to an energetic displacement towards higher binding energies of the corresponding peak in the $I(\uparrow\uparrow)$ spectrum when the photon energy is increased from 17.4 to 23.2 eV. In the experimental spectra (left-hand side of figure 15), the hybridization occurs as an energetic shift of the intensity weight of the peak in $I(\uparrow\uparrow)$ between 19.1 and 21.1 eV. Whereas at 19.1 eV the peak is asymmetrically shaped with higher weight on the low-binding-energy side, at 21.1 eV the weight is shifted to the side with higher binding energy.

This Δ_{7+} hybridization provides an excellent example of how the comparison of experimental MCDAD data to a fully relativistic photoemission calculation helps to identify even details of the spin-orbit- and exchange-split band structure. In reference [37] more such details are discussed. One other important point concerns the spectra at 11.1 eV photon energy. From figure 17 it can be seen that at this photon energy only the majority states are probed, since the minority Δ_{7+} and Δ_{6+} states are above the Fermi level and thus unoccupied close to the X point. Transitions from the majority Δ_{7-} and Δ_{6-} bands occur for opposite alignment of the photon helicity and magnetization directions. The energetic separation of the peaks observed at 11.1 eV photon energy in $I(\uparrow\uparrow)$ and $I(\uparrow\downarrow)$ therefore represents directly the energetic separation between the Δ_{7-} and Δ_{6-} bands at $k_{\perp} \approx 0.92 \pi/a$, i.e., it is a measure for Δ_{so} . The experimental value obtained thus for Δ_{so} at that point of the Brillouin zone is (50 ± 5) meV, as determined from the spectra of figure 15 [37].

The present example has shown how MCDAD data can deliver valuable information about the electronic structure. Comparison to fully relativistic calculations additionally provides the possibility of extracting specific information about the valence states, and helps to identify even fine details of the band structure in the experimental spectra.

4.1.2. Threefold symmetry: Co/Cu(111). In the previous section it was demonstrated that the origin of the D_{ex} -type magnetic dichroism can be related to transitions from different bands in the spin-orbit- and exchange-split band structure. In this section we will present another example of this correlation of magnetic dichroism with direct interband transitions, still using the totally symmetric geometry (figure 11). We will choose a system showing a threefold rotational symmetry, namely Co/Cu(111). In reference [48] it was demonstrated how measurements of magnetic circular dichroism in this geometry can be used to obtain information about the band structure even without support from theoretical photoemission calculations, just using the analytical results of Henk *et al* [45].

The growth of Co on Cu(111) is accompanied by three-dimensional island formation and stacking faults [49–51]. Whereas a perpendicular easy axis of magnetization was found only for very thin uncapped films, capping with Cu yielded a perpendicular magnetization up to 2 ML Co thickness [52,53]. The morphology of the Co films can be significantly improved by the use of Pb as a surfactant during deposition [54]. Pb predeposited on Cu(111) thereby floats on the surface during subsequent deposition of Co and Cu films [54]. The different morphology also influences the magnetic properties: in a capped Cu/Co/Cu(111) structure, grown with Pb as the surfactant, a perpendicular magnetization is found up to a Co film thickness of 3–4 ML [53]. In reference [48] a 1.5 ML Pb/2 ML Cu/3 ML Co/Cu(111) stack was therefore used for the investigation of the electronic states of perpendicularly magnetized Co ultrathin layers.

Before turning to the experimental results, we will consider the electronic states for normal electron emission from the threefold-rotational-symmetric (111) surface, i.e., along the Λ axis

of an fcc metal. Most of this parallels the analysis of the electronic states along the Δ axis given in the previous section, and will thus be discussed somewhat more briefly here.

The symmetry of the (111) surface is C_{3v} . Without spin-orbit coupling, electronic states along the Λ axis can be represented using the irreducible representations Λ^1 , Λ^2 , and Λ^3 . For normal light incidence, non-relativistic dipole selection rules allow only transitions from Λ^3 states into the Λ^1 final-state band [42]. In the presence of spin-orbit splitting, the spatial symmetry is no longer a good quantum number, but the non-relativistic selection rules remain valid in the sense that they are now only applicable to the portions of the bands which exhibit the corresponding spatial symmetry. The relativistic electronic states can be classified according to two irreducible representations of the double group, Λ_6 and $\Lambda_{4,5}$. The former is a two-dimensional representation, the latter a degenerate twin of two one-dimensional representations. The final-state band has Λ_6 symmetry, i.e., Λ_6^1 in the notation in which we append the predominant spatial symmetry as a superscript. The initial-state bands providing the photoemission signal for normal incidence, Λ^3 , split into pairs of Λ_6 and $\Lambda_{4,5}$ bands in the presence of spin-orbit coupling, which we will write as Λ_6^3 and $\Lambda_{4,5}^3$.

The presence of a perpendicular magnetization reduces the symmetry of the system, and lifts the Kramers degeneracy. The two-dimensional representation Λ_6 splits into a pair of one-dimensional representations, which can be labelled according to the time-reversal behaviour Λ_{6+} and Λ_{6-} , analogous to the Δ_6 or Δ_7 bands treated in the previous section. Without interband hybridization, the predominant spin character for Λ_{6+}^3 states is minority, and for Λ_{6-}^3 states majority. Again, we have to note that this assignment of time-reversal symmetry is not unique. For the $\Lambda_{4,5}$ states the situation is somewhat more complicated. They decompose into the two one-dimensional representations Λ_4 and Λ_5 , which both contain basis functions of both spin directions. To simplify the matter, the Λ_4 and Λ_5 bands are sometimes grouped together like in the non-magnetic case, and referred to as $\Lambda_{4,5+}^3$ and $\Lambda_{4,5-}^3$, following the treatment of the Λ_6 bands.

According to reference [45], the photoemission intensity for parallel and antiparallel alignment of the helicity and magnetization directions for the threefold-symmetric surface is

$$\begin{aligned} I(\uparrow\uparrow) &= 2|M_6^{+-}|^2 + |M_{4,5}^{-+}|^2 + |M_{4,5}^{--}|^2 \\ I(\uparrow\downarrow) &= 2|M_6^{-+}|^2 + |M_{4,5}^{+-}|^2 + |M_{4,5}^{++}|^2. \end{aligned} \quad (19)$$

The nomenclature for the matrix elements is similar to that in equation (18); for example, M_6^{+-} describes transitions from an initial state with Λ_{6-}^3 symmetry to a final state with Λ_{6+}^1 symmetry, and so on.

Figure 18 shows a fully relativistic band-structure calculation for fcc bulk Co along the Λ axis [55]. Bands with mainly minority character are represented as dotted lines, bands with mainly majority character as solid lines. Thick lines highlight bands with Λ_6 double-group representation and Λ_3 spatial symmetry. Although this calculation was done for an in-plane magnetization, we will use this band structure as a starting point for the discussion of the dichroism, and also for later comparison to the results for the ultrathin Co film. All of the labelling of the band symmetries in figure 18 is already as if it were for a perpendicular magnetization. The differences in band structure for in-plane and out-of-plane magnetizations are mainly restricted to the crossing points of the bands. The different symmetry representations of the bands in the two cases allow different bands to cross each other. The hybridizations by which forbidden degeneracies at some of the crossing points are lifted will thus be different in the case of perpendicular magnetization; on the Λ axis this will mainly affect the hybridization region around 1 eV binding energy on the right-hand side of figure 18 close to the Γ point, and the crossings of the sp-like Λ_{6+}^1 and Λ_{6-}^1 bands with the Λ_{6+}^3 and Λ_{6-}^3 bands, respectively.

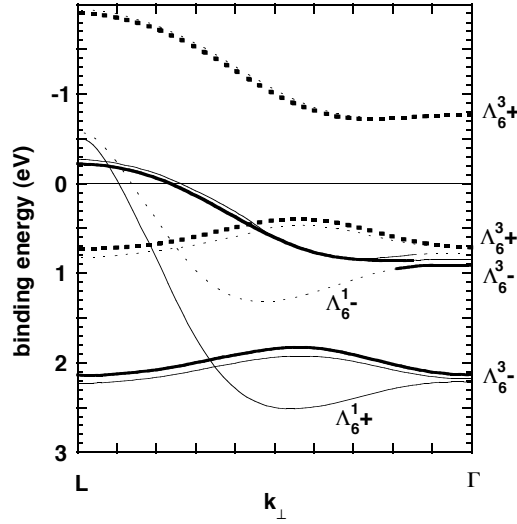


Figure 18. The fully relativistic band-structure calculation for fcc bulk Co along the Λ axis [55], calculated for in-plane magnetization, but labelled as if it were for a perpendicular magnetization. Dotted lines denote bands with mainly minority character, solid lines bands with mainly majority character. Thick lines highlight bands with Λ_6 double-group representation and Λ^3 spatial symmetry.

Two exchange-split pairs of bands with Λ^3 spatial symmetry can be observed in the energy range of figure 18. These are usually referred to as the ‘upper’ and ‘lower’ 3d bands. All four of these bands are further split by spin–orbit splitting, so a total of eight bands carries a predominant Λ^3 spatial symmetry. The upper minority band is completely above the Fermi level, and therefore unoccupied; the corresponding majority band crosses the Fermi energy close to the L point. We will see that in the experiment mainly the energy range between E_F and about 1.5 eV binding energy is accessed, because of the strong Cu valence band signal at higher binding energies. The experiment will therefore probe the lower minority and the upper majority bands, which show binding energies of less than 1 eV.

The final-state bands involved in the UV photoemission process result from the continuation of the two Λ_6^1 bands which reach the L point at about 0.5 eV above the Fermi level, and after forming a gap at the zone boundary are folded back into the first Brillouin zone. A free-electron parabola calculated for an inner potential of 10 eV shows that the bands cross the vacuum level about halfway between Γ and L. That means that the initial-state bands of the right-hand half of figure 18 will be probed, and that with increasing photon energy the probed k_\perp will be closer to the Γ point.

A schematic representation explaining the origin of the dichroism in that system is shown in figure 19. In the lower panel the energetic positions of the four bands with Λ^3 spatial symmetry which are present in the energy interval between E_F and $E_B = 1$ eV in the absence of hybridization are marked by vertical lines. The influence of the spin–orbit splitting is indicated by arrows. The line type of the bars is the same as for the respective bands in figure 18, i.e., majority bands are represented as solid lines, and minority bands as dotted lines. The observed dichroism is the intensity difference $D = I(\uparrow\uparrow) - I(\uparrow\downarrow)$. According to equation (19) the contribution of the Λ_6 bands to the dichroism is of the type $|M_6^{+-}|^2 - |M_6^{-+}|^2$. This means that, for a given light helicity, only bands with either Λ_{6+} symmetry or with Λ_{6-} symmetry contribute to the spectra. This is shown in the centre panel of figure 19, where

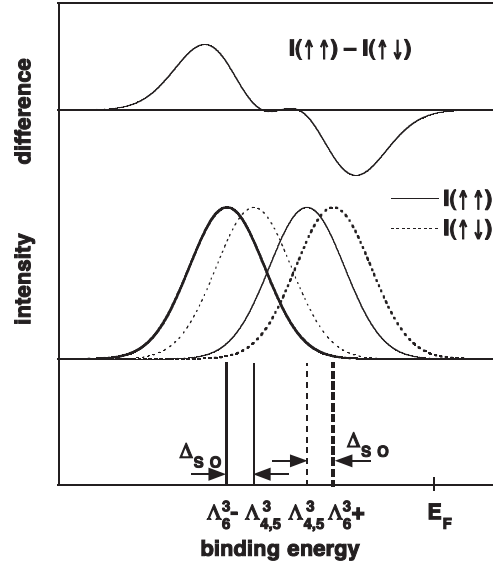


Figure 19. Bottom: a schematic representation of the four bands constituting the dichroism of Co(111) in the totally symmetric geometry. The arrows indicate the splitting due to spin-orbit interaction. Solid (dotted) lines represent band energetic positions of majority (minority) bands. Centre: schematic contributions to the intensity distribution curves for parallel (solid lines, $I(\uparrow\uparrow)$) and antiparallel alignment (dotted lines, $I(\uparrow\downarrow)$) of the photon spin and magnetization directions. Thick (thin) lines mark contributions of bands with Λ_6 ($\Lambda_{4,5}$) double-group symmetry. Top: the intensity difference $D = I(\uparrow\uparrow) - I(\uparrow\downarrow)$ of the spectra of the centre panel. Positive and negative peaks are located close to the energetic positions of Λ_{6-}^3 and Λ_{6+}^3 bands.

the thick solid and dotted curves schematically represent the spectral contribution of the Λ_6^3 bands for parallel and antiparallel alignment of the photon spin and magnetization directions, respectively. The alternating excitation of *different* transitions is again characteristic for the D_{ex} -type dichroism in the totally symmetric geometry.

The contribution from the $\Lambda_{4,5}$ bands is somewhat more complicated. From equation (19) there follows a contribution $|M_{4,5}^{-+}|^2 - |M_{4,5}^{++}|^2 + |M_{4,5}^{--}|^2 - |M_{4,5}^{+-}|^2$ to the dichroism. Unlike the case for the Λ_6 bands, transitions from both $\Lambda_{4,5+}$ and $\Lambda_{4,5-}$ states occur for each light helicity. As mentioned before, this is a consequence of the $\Lambda_{4,5\pm}$ representations not being irreducible. Neglecting the (small) exchange splitting in the final state between the Λ_{6+}^1 and Λ_{6-}^1 bands, the $\Lambda_{4,5}$ states should therefore not contribute to the dichroism, because their contributions to the difference cancel each other out [48]. Unfortunately, the assignment of $\Lambda_{4,5+}$ and $\Lambda_{4,5-}$ symmetries to the $\Lambda_{4,5}^3$ bands shown in the band structure of figure 18 or in the lower panel of figure 19 is not as straightforward as for the Λ_6^3 bands. To assess the role of these bands for the dichroism, it is easier to recall the condition that in the limit of vanishing spin-orbit coupling no dichroism should be observed. After having determined the contribution of the Λ_6^3 bands to the spectra $I(\uparrow\uparrow)$ and $I(\uparrow\downarrow)$, the contribution of the $\Lambda_{4,5}^3$ bands should be such that for $\Delta_{so} \rightarrow 0$ the difference $I(\uparrow\uparrow) - I(\uparrow\downarrow)$ becomes zero. This is the case for the curves shown in the centre panel of figure 19. Here, the thin solid and dotted curves mark spectral contributions of the bands for parallel and antiparallel alignment of the helicity and magnetization, respectively. If transitions from the $\Lambda_{4,5}^3$ minority band occur for parallel alignment $I(\uparrow\uparrow)$, as shown in figure 19, they will, in the limit of $\Delta_{so} \rightarrow 0$, compensate for the Λ_{6+}^3 contribution from $I(\uparrow\downarrow)$ to the difference $D = I(\uparrow\uparrow) - I(\uparrow\downarrow)$.

The resulting dichroism for $\Delta_{so} \neq 0$ is shown in the top panel. Because of the energetic proximity of the bands, the expected positive/negative/positive/negative structure is not present in the difference curve, and only the first positive and the last negative peak are prominent. They are positioned at about the binding energy of the Λ_6^3 bands, with the positive peak close to the Λ_{6-}^3 band, and the negative peak close to the Λ_{6+}^3 band. Peaks observed in difference spectra can thus be used to identify the contributions of different bands to the total photoemission signal.

Figure 20 shows a series of experimental dichroism measurements for different photon energies $h\nu$ from reference [48]. On the left-hand side photoemission intensity curves for parallel ($I(\uparrow\uparrow)$, solid lines) and antiparallel alignment of the photon spin and sample magnetization ($I(\uparrow\downarrow)$, dotted lines) are depicted. The peak which disperses from 0.3 eV binding energy at $h\nu = 8$ eV to 0.9 eV binding energy at $h\nu = 24$ eV is attributed to emission from Co 3d states, as discussed above. The increase of intensity at the high-binding-energy end of most of the spectra marks the onset of emission from Cu 3d states, which is expected at binding energies above 2 eV [16,43]. Conventional photoemission would just deliver the sum $I(\uparrow\uparrow) + I(\uparrow\downarrow)$. From that alone, a separation of the two (twinned) contributing bands would be nearly impossible. Magnetic dichroism, in contrast, allows the precise separation of bands with different double-group symmetries, and its differential nature makes it widely insensitive to non-magnetic contributions from cap layers or the substrate.

The right-hand side of figure 20 shows the experimental dichroism, i.e., the differences between the spectra on the left-hand side, magnified in intensity by an (arbitrary) factor of 5. Circles represent the data, and solid lines are smoothing splines for the data [48]. A positive peak at higher binding energies, and a negative peak at lower binding energies can be made out in all of the difference spectra. The positions are marked by small vertical bars. It is easy to see how these two peaks correspond to the schematic explanation of figure 19. Their dispersion can therefore be used to map the dispersion of the Λ_{6+}^3 and Λ_{6-}^3 bands, which for small spin-orbit splitting are representative for the dispersion of the lower minority and the upper majority band, respectively. The experimental dispersion obtained thus from the dichroism spectra is shown in figure 21. Solid upward-pointing (downward-pointing) triangles are plotted at the binding energies of the positive (negative) peaks in the difference spectra versus the value of k_{\perp} [48]. The latter was obtained by assuming a simple free-electron-like final-state dispersion with an inner potential of 10 eV. The solid and broken lines serve as guides to the eye. The inset shows again the band-structure calculation of Ebert from figure 18 [55]. Comparing the experimental points with the calculated band structure, the band-structure origin of the magnetic circular dichroism, as outlined before, becomes immediately obvious. The dispersion of the positive and negative peaks of the difference spectra displays directly the dispersion of the lower minority Λ_{6+}^3 and the upper majority Λ_{6-}^3 bands marked by an ellipse in the inset of figure 21.

No significant narrowing of the bands with respect to the bulk band structure is observed in the experiment. This and the strong dispersion of the bands for a film of only 3 ML can be explained by hybridization between substrate and film states continuing the Bloch periodicity [48]. The main differences between the experiment and the calculation concern the energetic separation between the upper majority and the lower minority d bands. In the experiment, close to the Γ point they are separated by 0.5 eV; in the calculation only by 0.2 eV. One has to keep in mind, however, that the experimental peak positions do not exactly coincide with the positions of the spin-orbit-split pair of bands, but are slightly outside these (cf. figure 19). On the other hand, the main differences between experiment and theory can be attributed to the influence of finite thickness, hybridization with Cu d states, and modified lattice properties due to the sandwiching between Cu layers.

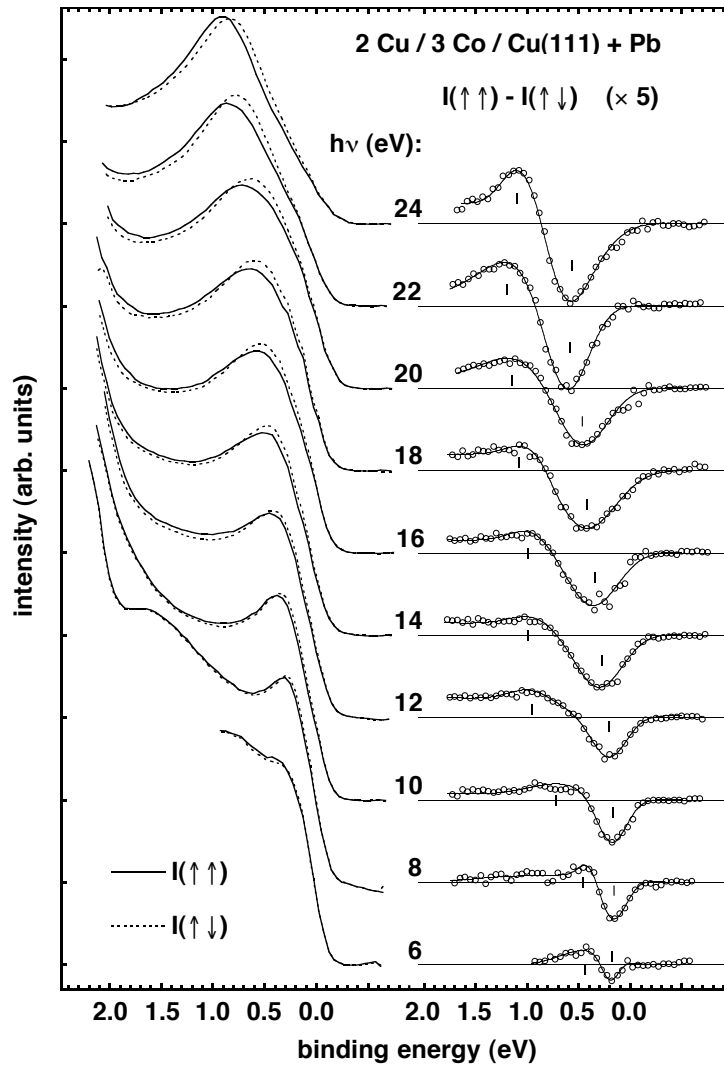


Figure 20. Left: a series of partial intensity spectra of 2 ML Cu/3 ML Co/Cu(111), grown with Pb as the surfactant, for different photon energies $h\nu$. Shown are spectra for parallel (solid lines) and antiparallel alignment (dotted lines) of the photon spin and magnetization directions. Right: differences between the partial spectra on the left-hand side, scaled by a factor of 5 (circles). The solid lines are smoothing splines for the data. The small vertical bars mark peak positions of positive and negative peaks. (From reference [48].)

The present example of Cu/Co/Cu(111) again demonstrated that the analytical expressions of Henk *et al* [45], which link peaks in the dichroism spectra to the symmetry of initial-state valence bands in the picture of direct interband transitions, are appropriate for the conclusive and consistent interpretation of magnetic dichroism in valence band photoemission. Using circular polarization in the totally symmetric geometry, these analytical rules describe the selective excitations of transitions from different initial-state valence bands, which makes the information content of the dichroism measurements nearly as valuable as that of explicitly spin-resolved measurements.

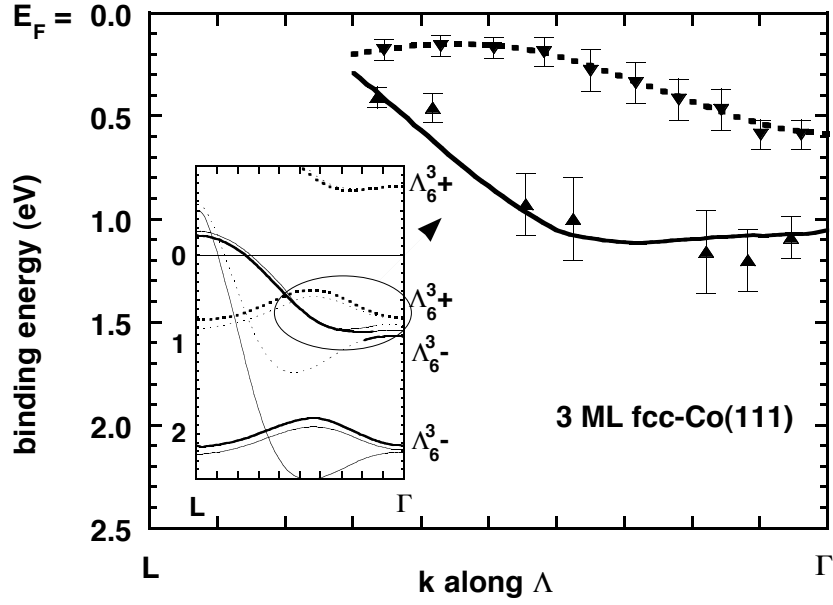


Figure 21. A plot of the peak positions of the difference spectra from figure 20 as a function of electron wavevector perpendicular to the surface. Upward-pointing (downward-pointing) triangles denote positions of positive (negative) peaks of the difference spectra. The k -values are for free-electron-like final states with an inner potential of 10 eV. The lines are guides to the eye. The inset shows the band-structure calculation of figure 18 [55] for comparison. The region probed by the experiment is indicated by an ellipse. (From reference [48].)

4.2. Normal emission, linear polarization, in-plane magnetization

4.2.1. Twofold symmetry: Fe/W(110). In this section we will discuss an experimental example of the application of linear dichroism. As mentioned in section 3, a geometry like the one shown in figure 7 is very common for the measurement of linear dichroism. The dichroism is measured upon reversal of the magnetization direction, which is switched from ‘up’ to ‘down’ with respect to the reaction plane of light incidence and electron emission. This geometry has the advantage that a parasitic circular polarization does not produce any circular magnetic dichroism because of symmetry constraints (cf. figure 7, ‘reflection at $x-z$ ’). We will discuss a joint experimental and theoretical study of the linear magnetic dichroism in valence band photoemission from ultrathin Fe films performed by Rampe *et al* [56]. 15 ML Fe(110) films, grown on a W(110) substrate, served as the magnetic sample. At that film thickness, the topmost layers of the film consist of (110)-oriented bcc Fe with the lattice constant of bulk Fe [56].

The geometry of the experiment is shown in figure 22. $x-z$ and $y-z$ are mirror planes of the crystal. Here, x is oriented along the $[001]$, and y along the $[\bar{1}10]$ in-plane azimuth direction. The light is linearly polarized in the $[\bar{1}10]$ plane, and impinges on the crystal surface at under 45° in the $[001]$ azimuth direction (p polarization). The magnetization is switched between $[\bar{1}10]$ ($M+$) and $[1\bar{1}0]$ ($M-$). Photoelectrons are collected in normal emission. For (110) surfaces, this probes electronic states on the Σ axis, which is the axis along the surface normal in reciprocal space.

The way that we will handle the analytical description of the present example is exactly analogous to our procedure in the previous two sections. First we consider the band symmetries

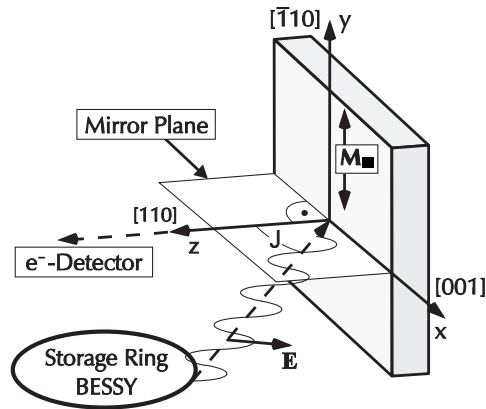


Figure 22. The geometry for the measurement of linear magnetic dichroism at the (110) surface of a cubic crystal. The magnetization is along the $[\bar{1}10]$ ($M+$) or $[\bar{1}\bar{1}0]$ ($M-$) direction. p-polarized light impinges at a polar angle $\vartheta = 45^\circ$ in the [001] azimuth direction onto the surface. Electrons are detected in normal emission. (From reference [56].)

of the non-magnetic case in the limit of vanishing spin-orbit interaction. This will tell us the spatial symmetry of the states, which is required for dipole transitions in the geometry used in the experiment. Next we evaluate the influence of spin-orbit coupling, and of a remanent magnetization on the symmetry character of the bands. The appropriate analytical formulae of reference [45] will then provide a means for interpretation of the dichroism spectra. In addition, fully relativistic photoemission calculations have been performed and the results compared to the experimental data in reference [56], which further facilitates the correlation of experiment and theory, and corroborates the analytical formulae.

The point group of the non-magnetic sample in the geometry of figure 22 is C_{2v} . Its single group has four irreducible representations, Σ^1 , Σ^2 , Σ^3 , and Σ^4 . Dipole selection rules for transitions into the Σ^1 final-state band depend on the light polarization: for a component of the polarization vector along the [110] surface normal (ideally grazing incidence), electrons from Σ^1 initial states are excited; for a component along the [001] in-plane direction (normal incidence, polarization vector in the [001] azimuth direction), electrons from Σ^3 initial states are excited [42]. For off-normally p-polarized light in between these two extremes (figure 22), the light polarization contains both components, so both initial states with either Σ^1 or Σ^3 spatial symmetry contribute to the photoemission signal.

The corresponding relativistic double group contains only one irreducible representation, Σ^5 . In the notation with the single-group symmetry as superscript, bands can be labelled according to their predominant spatial symmetry, by Σ_5^1 , Σ_5^2 , Σ_5^3 , or Σ_5^4 . The effect of spin-orbit coupling on the band structure is to lift all degeneracies at band crossings by inducing hybridizations, since all bands exhibit the same double-group symmetry, and are thus not allowed to cross each other.

In the presence of a magnetization, the bands are split by the exchange splitting. It is instructive to consider the non-relativistic case first, because then it is easier to see how the magnetic double-group symmetry correlates with the single bands in the band structure. In the absence of spin-orbit coupling the electron spin is a good quantum number, and we can write the exchange-split bands as $\Sigma^{i\uparrow}$ for majority-spin bands, and $\Sigma^{i\downarrow}$ for minority-spin bands, where $i = 1, 2, 3, 4$. Up to here, we have not yet considered the direction of the magnetization. For the magnetization along an in-plane symmetry axis, the symmetry of the whole system is

lower than for a perpendicular magnetization. In the present example it is lowered to C_s . Its double group has two irreducible representations, which we will label γ_+ and γ_- , following references [31, 56]. The correlation of the spin and orbital parts of the wavefunctions with these symmetry representations can be formulated as

$$\begin{aligned}\Sigma^{1\uparrow}, \Sigma^{2\downarrow}, \Sigma^{3\uparrow}, \Sigma^{4\downarrow} &\longrightarrow \gamma_+ \\ \Sigma^{1\downarrow}, \Sigma^{2\uparrow}, \Sigma^{3\downarrow}, \Sigma^{4\uparrow} &\longrightarrow \gamma_-\end{aligned}\quad (20)$$

In the present case, where transitions from states with Σ^1 or Σ^3 spatial symmetry exclusively constitute the photoemission signal, this means that initial states with predominant majority spin have γ_+ double-group representation, initial states with predominant minority spin γ_- . Again, we will append the spatial symmetry as a superscript to the double-group symmetry, and write $\gamma_+^1, \gamma_-^1, \gamma_+^2$, etc.

In reference [45] the corresponding analytic formula for the photoemission intensities $I(M+)$ and $I(M-)$ can be found:

$$\begin{aligned}I(M\pm) = &(\sin^2 \vartheta)(|M^{1++}|^2 + |M^{1--}|^2) + (\cos^2 \vartheta)(|M^{3++}|^2 + |M^{3--}|^2) \\ &\pm (\sin \vartheta)(\cos \vartheta) \operatorname{Im}(M^{1++*} M^{3++} - M^{1--*} M^{3--}).\end{aligned}\quad (21)$$

The nomenclature of the matrix elements is like in the previous two sections: M^{1++} describes transitions from γ_+^1 initial states into γ_+^1 final states, M^{3--} transitions from γ_-^3 initial states into γ_-^3 final states, and so on. ϑ is the angle of light incidence with respect to the surface normal. (Strictly speaking, it is the angle of light propagation inside the crystal. We will see later that in fact there may be a significant difference between inside and outside of the sample.) The first two terms in equation (21) describe the angle dependence of direct transitions, which reflect the non-relativistic dipole transition rules as mentioned before: for normally incident light ($\sin \vartheta = 0$), only transitions from states with Σ^3 spatial symmetry occur; for ideally grazing incidence ($\cos \vartheta = 0$), only transitions from states with Σ^1 spatial symmetry occur. The squares of the matrix elements identify them as describing intensities of direct transitions. They are, however, not the source of the dichroism, since they occur identically in $I(M+)$ and $I(M-)$, and thus do not contribute to the difference $D = I(M+) - I(M-)$. D is made up solely of the third term, which originates from the mixing of these two cases, and additionally contributes to the photoemission signal. The product of different matrix elements describes the interference between excitations induced by light polarization components in the x - and in the z -direction. It is maximum for $\vartheta = 45^\circ$, where the contributions from the Σ^1 and Σ^3 states are equally large, and vanishes at $\vartheta = 0^\circ$ and $\vartheta = 90^\circ$, where only one of them is present.

This, being caused by the interference between two excitation channels, is the main characteristic of linear (or unpolarized) magnetic dichroism. It distinguishes linear dichroism from the two examples of circular dichroism of the previous two sections, where the dichroism was proportional to the squares of matrix elements (cf. equations (18), (19)). In practice, that means that it is necessary to have simultaneously transitions from γ_+^1 and γ_+^3 initial states, or from γ_-^1 and γ_-^3 initial states to observe a dichroism. At a certain photoelectron energy this is precisely the case if there is a hybridization between states with Σ^1 and Σ^3 spatial symmetry, resulting in the simultaneous presence of both. The observed dichroism will thus be a measure for such hybridizations, and will be maximum at the energetic positions of lifted degeneracies between either γ_+^1 - and γ_+^3 -bands, or γ_-^1 - and γ_-^3 -bands.

The calculated fully relativistic band structure of bulk Fe along the Σ axis from reference [56] is shown in figure 23. For the sake of clarity, bands with γ_+ double-group symmetry are depicted on the left-hand side, and bands with γ_- double-group symmetry on the right-hand side. Bands are labelled in addition according to their predominant spatial and spin symmetry.

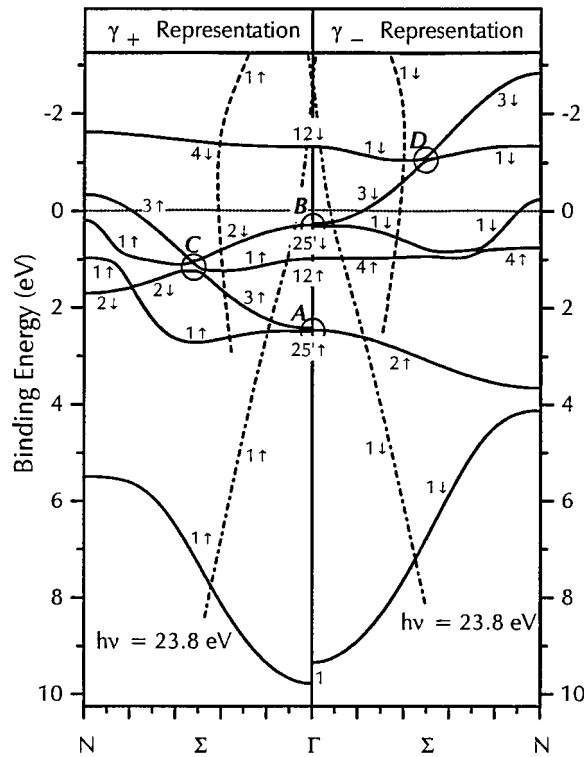


Figure 23. The calculated fully relativistic valence band structure of Fe along the Σ axis. The bands are printed on the right-hand or left-hand side according to their double-group symmetry, γ_+ or γ_- . The labels on the bands indicate the predominant spatial and spin symmetry. Final-state bands, shifted down in energy by 23.8 eV, are displayed as dash-dotted and dashed lines. Circles denote regions of hybridization due to forbidden degeneracies between bands with Σ^1 and Σ^3 spatial symmetry. (From reference [56].)

To illustrate at which k_{\perp} the initial-state bands are probed in the experiment, the final-state bands, shifted down in energy by 23.8 eV, are displayed as dash-dotted and dashed lines. The latter mark final-state bands which have their origin at a Γ point off the axis that we are looking at, and are highly damped. Transitions for a photon energy of 23.8 eV will thus mainly occur at the crossings between initial states and the final states represented by dash-dotted lines in figure 23. As outlined before, magnetic linear dichroism is expected for a mixing of Σ^1 and Σ^3 spatial symmetry. There are four regions in the band structure along the Σ axis where this is the case. They are marked by small circles in figure 23, and labelled A to D. Of these four, only A–C are below the Fermi level E_F and occupied. The top panel of figure 24 shows a more detailed view of the hybridizations B and D of the γ_+ -bands.

The inset displays a magnified reproduction of region B. The two bands which form the hybridization at B are highlighted by thick lines and labelled ‘Band I’ and ‘Band II’. The calculated spatial and spin symmetry characters of these bands are shown in the lower panels as functions of k_{\perp} along Σ . Close to the Γ point, each band has about 50% Σ^1 and 50% Σ^3 spatial symmetry. Up to $k_{\perp} = 0.2\pi/a_{\perp}$ both bands have sizable admixtures of Σ^1 and Σ^3 spatial symmetry, before at higher k_{\perp} band I becomes nearly exclusively of Σ^3 , and band II of Σ^1 spatial symmetry. At even higher k_{\perp} -values, both bands hybridize with bands of Σ^4 symmetry, which however is irrelevant for the dichroism in our present example.

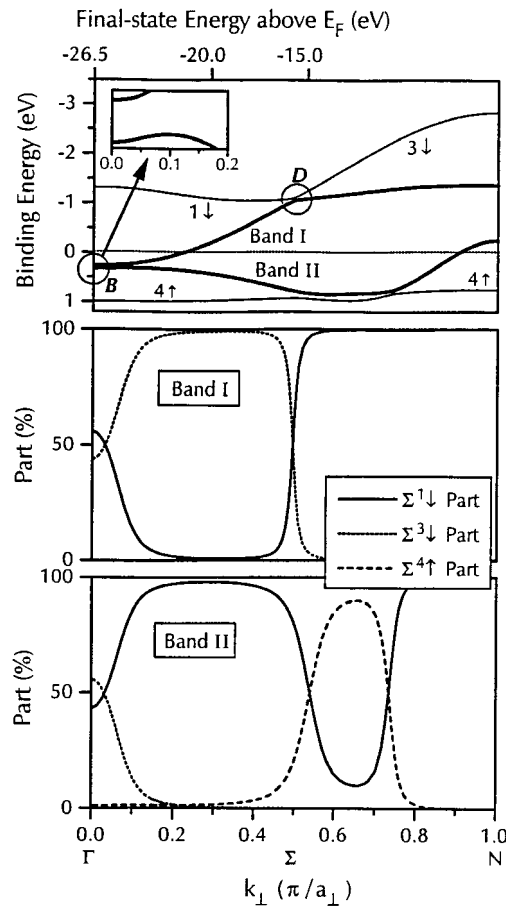


Figure 24. Top: a detailed view of the γ_{\perp} -part of the band structure around the Fermi energy. The inset displays a magnified reproduction of the region labelled B. Two bands which hybridize at B are highlighted by thick lines. Centre and bottom: calculated spatial and spin symmetry characters of the bands labelled 'Band I' and 'Band II' in the upper panel as functions of k_{\perp} along Σ . The simultaneous presence of Σ^1 and Σ^3 spatial symmetry in both of these bands close to Γ is clearly seen. (From reference [56].)

Dichroism from the hybridization at B should consequently be strongest if the transitions occur between Γ and $k_{\perp} = 0.2\pi/a_{\perp}$. From figure 23 it can be seen that at a photon energy about 1.7 eV lower than 23.8 eV the transitions close to the Fermi energy reach a k_{\perp} -value of about $0.2\pi/a_{\perp}$ close to the Fermi energy, and occur closer to Γ for increasing photon energy. This should manifest itself in the observed dichroism: around 0.3 eV binding energy the dichroism should be most pronounced at these photon energies. In addition, there should also be dichroism at about 2.6 eV binding energy, with a maximum in the photon energy dependence around $h\nu = 23.8 + 4$ eV (from hybridization A), and at 1 eV binding energy for photon energies around $23.8 - 8$ eV (from hybridization C).

In figure 25, the experimental and theoretical photoemission spectra series for 15 ML Fe/W(110) for different photon energies are depicted on the left-hand and right-hand side, respectively. Spectra for magnetization along y ($M+$) are represented by solid lines, spectra for magnetization along $-y$ ($M-$) as dotted lines. Let us first focus on the theoretical spectra

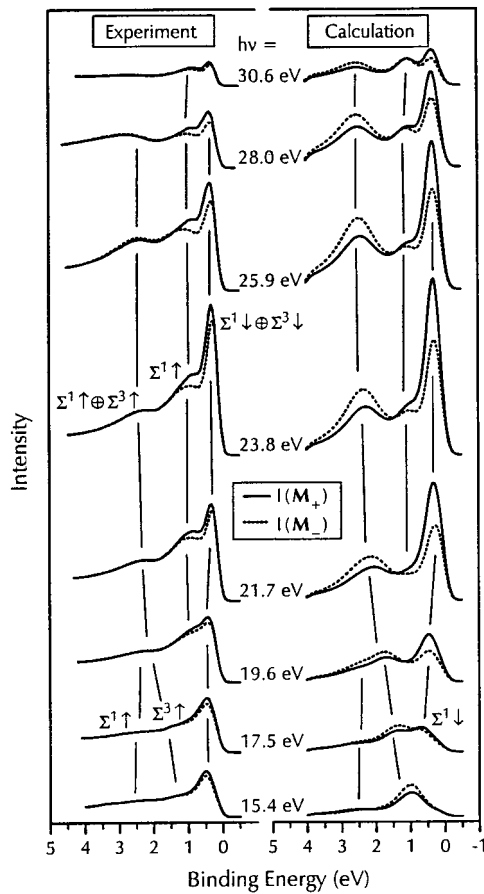


Figure 25. Series of partial intensity spectra of 15 ML Fe/W(110) for different photon energies $h\nu$, as indicated. Shown are spectra for the magnetization along $[1\bar{1}0]$ ($M+$, solid lines) and for the magnetization along $[1\bar{1}\bar{0}]$ ($M-$, dotted lines). Left: experimental spectra; right: theoretical spectra. The vertical lines indicate the dispersions of different peaks. (From reference [56].)

on the right-hand side. In most of the spectra two or three peaks can be distinguished; their dispersions are indicated by vertical lines. For the lowest photon energy (15.4 eV) the bands are probed around the centre of the Brillouin zone, for increasing $h\nu$ closer to Γ (cf. figure 23). Comparing the peak dispersion in the calculated spectra of figure 25 with the dispersion of the bands of Σ^1 or Σ^3 spatial symmetry of figure 23, the following correlation can be established: the peaks which remain constant at binding energies around 1 and 2.5 eV are caused by transitions from $\Sigma^{1\uparrow}$ bands, the dispersing feature between $E_B = 1$ eV at $h\nu = 15.4$ eV and $E_B = 2.5$ eV at $h\nu = 21.7$ eV stems from the $\Sigma^{3\uparrow}$ band between C and A, and the peak with the lowest binding energy below 1 eV is due to emission from $\Sigma^{1\downarrow}$ and $\Sigma^{3\downarrow}$ bands ('Band I' and 'Band II' in figure 24). All spectral features in the calculated spectra can thus be attributed to direct transitions in the relativistic band structure.

The corresponding peaks are also observed in the experimental spectra (left-hand side of figure 25), at slightly different binding energies. Other differences between experiment and theory concern the relative magnitude of the peaks, and details of the peak dispersion: whereas, for example, in the calculated spectra the $\Sigma^{1\uparrow}$ peak at 1 eV binding energy is clearly

separated from the $\Sigma^{1\downarrow}$ and $\Sigma^{3\downarrow}$ contributions at 0.5 eV binding energy only at photon energies of 23.8 eV and higher, in the experimental spectra two distinct peaks can be made out already at $h\nu = 19.6$ eV.

All of the peaks show dichroism, i.e., an intensity difference between the spectra for $M+$ and $M-$. It is more pronounced in the theoretical spectra, and exhibits a clear photon energy dependence. At 1 eV binding energy, the strongest dichroism in the theoretical spectra occurs at $h\nu = 15.4$ eV. This is in accordance with the above discussion, and is correlated with emission from the hybridization at C in figure 23. The peak at 2.5 eV binding energy exhibits the strongest dichroism for $h\nu = 23.8$ and 25.9 eV; this can be correlated with the hybridization at A. The most prominent peak at 0.5 eV in the theoretical spectra, finally, shows a pronounced dichroism for photon energies between 19.6 and 28.0 eV, which is strongest at $h\nu = 23.8$ eV. This is attributed to the hybridization at B.

The same photon energy dependence of the dichroism from hybridizations at A and B is observed also in the experimental spectra. At 2.5 eV binding energy a sizable dichroism is seen only for $h\nu = 23.8$ eV; at 0.5 eV binding energy the dichroism is maximum for $h\nu = 23.8$ and 25.9 eV. A photon energy dependence of the dichroism resulting from the hybridization at C is not observed in the experimental spectra. The reason for this could be that the dispersion of the final-state band in the experiment is somewhat different to that in the calculation: the peaks due to emission from the $\Sigma^{1\uparrow}$ and $\Sigma^{3\uparrow}$ bands which hybridize at C are merging in the theoretical spectra for 15.4 eV photon energy, whereas in the experiment they are still separated at the same photon energy. Probably the photon energy in the experiment has to be lowered further in order to observe the corresponding maximum of the dichroism.

A plot of the photoemission intensity of the 0.5 eV binding energy peak is shown in the upper panel of figure 26. The intensity of the experimental curves is depicted by solid symbols, the intensity of the theoretical curves by open symbols. Both are shown scaled with respect to each other to coincide at 23.8 eV photon energy. The lower panel gives the dependence of the corresponding dichroic difference in that peak. The theoretical differences are plotted on a vertical scale enhanced by a factor of 5 with respect to the intensities, the experimental differences on a scale enhanced by a factor of 10. A clear maximum around a photon energy of 24 eV can be distinguished in both experiment and theory. This confirms the above discussion, and demonstrates the origin of the dichroism in that particular peak as being due to the coherent emission from $\Sigma^{1\downarrow}$ and $\Sigma^{3\downarrow}$ states, as explained in figure 24.

From figure 25 it can be seen that the difference $D = I(M+) - I(M-)$ is positive at the lowest binding energies, where the dichroism is attributed to $\Sigma^{1\downarrow}/\Sigma^{3\downarrow}$ hybridization at B, and negative at higher binding energies, where it is attributed to $\Sigma^{1\uparrow}/\Sigma^{3\uparrow}$ hybridization at A and C. Recalling equation (21), D is proportional to the imaginary part of $M^{1++}M^{3++} - M^{1--}M^{3--}$. Although on the basis of analytical analysis alone, no statements about the signs of the products of the matrix elements can be made, in the present example it seems that $\text{Im}(M^{1++}M^{3++})$ and $\text{Im}(M^{1--}M^{3--})$ show the same sign in the photon energy range covered here. This leads to the opposite sign of D caused by $\Sigma^{1\uparrow}/\Sigma^{3\uparrow}$ states (described by $\text{Im}(M^{1++}M^{3++})$) and by $\Sigma^{1\downarrow}/\Sigma^{3\downarrow}$ states (described by $\text{Im}(M^{1--}M^{3--})$).

The present example has demonstrated that magnetic linear dichroism can be explained qualitatively by the analytical theory, considering direct transitions in the exchange- and spin-orbit-split band structure. The agreement of the experimental results with fully relativistic photoemission calculations proves that this theoretical description of the dichroism is adequate. For excitation with linearly polarized light, the dichroism occurs as a consequence of interference in the coherent superposition of different excitation channels caused by different polarization components. The dependence of the dichroism on hybridization properties of the initial-state bands helps to adjust theoretical band structures to experimental observations, and

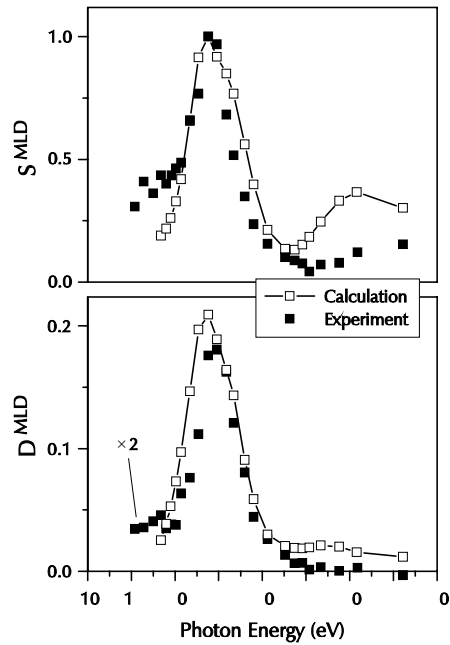


Figure 26. The photon energy dependence of the photoemission intensity (upper panel) and dichroic difference (lower panel) of the spectra of figure 25 at 0.5 eV binding energy. Solid symbols mark experimental points, open symbols theoretical points. The intensities in the upper panel are scaled in order to coincide at 23.8 eV photon energy. The y-axis scale of the lower panel is enhanced by a factor of 5 with respect to the upper panel; within that, experimental differences have been multiplied by a factor of 2. (From reference [56].)

to identify critical points in the band structure. Spin-orbit-induced band gaps or hybridization zones in the band structure can be probed by measuring the photon energy dependence of the linear dichroism.

4.2.2. Fourfold symmetry: Co/Cu(100). The previous example is very instructive as regards seeing how the dichroism depends on the interference between transition channels excited by different components of the light polarization. Other common geometries involving an in-plane magnetization can be analysed in a very similar way. A magnetization along an in-plane easy axis lowers the rotational symmetry of the crystal surface. An in-plane-magnetized sample with fourfold *crystalline* symmetry is therefore also described by the twofold point group C_{2v} , like in the previous example. The same analytical formula (equation (21)) describing linear dichroism will therefore be applicable. The only difference concerns the nomenclature for the electronic states involved, when we append the spatial symmetry of the non-magnetic case to label the bands for the magnetic relativistic case. Normal emission from a fourfold (100) surface of an fcc crystal probes the electronic states along the Δ axis, the spatial symmetry basis functions of which are Δ^1 , Δ^1 , Δ^2 , Δ^2 , and Δ^5 (compare section 4.1). In an experimental geometry like that in figure 22 a light polarization component in the x -direction can excite only dipole-allowed transitions from initial states with Δ^5 spatial symmetry, a light component in the z -direction only dipole-allowed transitions from initial states with Δ^1 spatial symmetry [42]. The double group of the magnetic sample is identical to that of the previous example, having the two irreducible representations γ_+ and γ_- . Like for equation (20), there exist correlations

between the spin and orbital parts of the wavefunctions within these symmetry representations:

$$\begin{aligned}\Delta^{1\uparrow}, \Delta^{1\downarrow}, \Delta^{2\downarrow}, \Delta^{2'\uparrow}, \Delta^{5\uparrow}, \Delta^{5\downarrow} &\longrightarrow \gamma_+ \\ \Delta^{1\downarrow}, \Delta^{1'\uparrow}, \Delta^{2'\uparrow}, \Delta^{2'\downarrow}, \Delta^{5\uparrow}, \Delta^{5\downarrow} &\longrightarrow \gamma_-\end{aligned}\quad (22)$$

Because the Δ^5 representation of the single group is two dimensional, its two components, whose degeneracy is lifted by spin-orbit coupling, contribute to both representations of the double group. In the given geometry only states with Δ^1 or Δ^5 spatial symmetry contribute to the photoemission signal. Equation (21), formulated for electronic states along the Δ axis, now reads

$$\begin{aligned}I(M\pm) = &(\sin^2 \vartheta)(|M^{1++}|^2 + |M^{1--}|^2) + (\cos^2 \vartheta)(|M^{5++}|^2 + |M^{5--}|^2) \\ &\pm (\sin \vartheta)(\cos \vartheta) \operatorname{Im}(M^{1++*} M^{5++} - M^{1--*} M^{5--}).\end{aligned}\quad (23)$$

Here ϑ is again the angle with respect to the surface normal of the incident light (inside the crystal), and the nomenclature for the matrix elements is again such that, for example, M^{5++} describes transitions from γ_+ initial states with Δ^5 spatial symmetry into γ_+ final states with Δ^1 spatial symmetry, etc. The first two terms describe the angular dependence of the photoemission signal, being composed of contributions from states with Δ^1 and Δ^5 spatial symmetry, as mentioned above. The third term describes the interference between these two contributions, which are excited by different components of the light polarization. This term is the one contributing to the dichroism. Whereas at the (110) surface the hybridization between Σ^1 and Σ^3 states of like double-group symmetry is necessary to evoke linear magnetic dichroism, in the case of the (100) surface it is the Δ^1/Δ^5 hybridization.

An example in the literature of such a geometry is found in reference [57]. There, unpolarized light from a He laboratory source was used to study photoemission from a Co/Cu(100) sample. Unpolarized light can be thought of as being incoherently composed of s- and p-polarized light. Since the s component does not contribute to the dichroism [45], in the given geometry the magnetic dichroism obtained with unpolarized light is qualitatively identical to the dichroism obtained with linearly polarized light, and described by the third term of equation (23). Fanelsa *et al* compared the experimental dichroism with fully relativistic band-structure and photoemission calculations, and found that hybridization between Δ^1 and Δ^5 minority states is indeed the cause of the dichroism [57].

4.3. Normal emission, circular polarization, in-plane magnetization

There are examples in the literature in which magnetic circular dichroism was measured for in-plane-magnetized samples [10,58,59]. As we have seen in the previous section, the analysis of fourfold- and twofold-symmetric crystal surfaces is straightforwardly identical for in-plane-magnetized samples. We will restrict consideration therefore to a fourfold-symmetric fcc (100) surface, where the symmetry representations are as in the previous example. Using again the geometry displayed in figure 22, the appropriate analytical formula from reference [45] yields for circular polarization the following dichroism upon magnetization reversal:

$$\begin{aligned}I(M\pm) = &(\sin^2 \vartheta)(|M^{1++}|^2 + |M^{1--}|^2) + (\cos^2 \vartheta)(|M^{5++}|^2 + |M^{5--}|^2) \\ &\pm (\sin \vartheta)(\cos \vartheta) \operatorname{Im}(M^{1++*} M^{5++} - M^{1--*} M^{5--}) + |M^{5+-}|^2 + |M^{5-+}|^2.\end{aligned}\quad (24)$$

As discussed in section 3, reversal of the light helicity does not result in a magnetic dichroism in that geometry. The first three terms of equation (24) are identical to equation (23). The fourth and fifth terms describe excitation by the light polarization component in the y -direction. It involves the spin-orbit-split twins of the initial states of the second term, as can be seen by the different sign of the corresponding final-state bands. Once more the dichroism

results from just the third term, and is caused by the interference between transitions excited by the x - and z -components of the light polarization vector. Qualitatively there is thus no difference between the dichroism measured with linearly and circularly polarized light in that geometry.

Using the geometry with the magnetization along x , as shown in figure 6, the dichroism upon magnetization reversal or upon light helicity reversal is identical, because the two operations result in equivalent geometries (cf. section 3). In that case the dichroism is described by the analytical formula [45]

$$I(M\pm) = I(\sigma\pm) = (\sin^2 \vartheta)(|M^{1++}|^2 + |M^{1--}|^2) + (\cos^2 \vartheta)(|M^{5+-}|^2 + |M^{5-+}|^2) \\ \pm 2(\sin \vartheta) \operatorname{Re}(M^{1++*} M^{5++} - M^{1--*} M^{5--}) + |M^{5++}|^2 + |M^{5--}|^2. \quad (25)$$

The last term describes again the excitation by the y -component of the circularly polarized light, and therefore does not depend on the angle of incidence ϑ . Because the quantization axis is now in the x -direction, the role of the second and fourth/fifth term on the right-hand side of equation (25) is interchanged with respect to equation (24). The third term is once more the one responsible for the dichroism. As before, it is a pure interference term, describing the interference between transitions from Δ^1 initial states excited by the z -component of the light polarization, and transitions from Δ^5 initial states excited by the y -component of the light polarization. Here the real part of the respective interference matrix element is probed, so there is a qualitative difference in dichroism with respect to the geometry where \vec{M} is along y . This is also reflected in a different angular behaviour. Since the transitions from Δ^5 initial states involved are based on the y -component of the exciting light, they do not depend on the angle of incidence. The angular dependence of the effect is thus simply like $\sin \vartheta$, reflecting the angular dependence of the photoemission from the Δ^1 part of the matrix element. The maximum of the effect is found by choosing the light incidence to be as near grazing as possible, i.e., to align the photon spin most widely with the magnetization direction, whereas in the previous example a light incidence close to 45° will result in a maximum dichroism.

4.4. Off-normal emission

In the previous sections we were able to correlate the magnetic dichroism in valence band photoemission spectra with the relativistic band structure by using the analytical formulae of reference [45] (cf. equations (18), (19), (21), (23)–(25)). These formulae take advantage of the symmetry character of the electronic valence states along the high-symmetry direction represented by the surface normal. For off-normal emission, the situation is somewhat more complicated. Firstly, most of the available band-structure calculations have been carried out for electronic states along high-symmetry directions in reciprocal space. It is thus not easy to find a theoretical band structure as input for the interpretation of experimental results. Secondly, the correlation of the observed features with certain electronic states without relativistic photoemission calculations is also not straightforward. There are some examples in the literature, however, where valence band magnetic dichroism in off-normal emission has been used for the investigation of electronic properties. We will in the following briefly review these, and focus on the points which are most important for future applications of magnetic dichroism in off-normal valence band photoemission.

In section 3 we discussed the feature that in the general case of photoemission from magnetic samples in low-symmetry experimental geometries there are four inequivalent spectra which can be obtained by reversing the magnetization or the light polarization. For linearly polarized light, ‘reversing’ therefore means changing the azimuth of incidence by 180° . The three quantities D_{ex} , D_{mag} , and D_{pol} have been defined on the basis of the differences between

these four spectra. D_{ex} represents the part of the dichroism which is identically obtained from the reversal of either magnetization or polarization (equation (14)), D_{mag} represents the part of the dichroism which occurs upon magnetization reversal only (equation (15)), and D_{pol} represents the part of the dichroism which is observed only on reversing the light polarization (equation (16)).

The latter exists also in photoemission from non-magnetic samples. An illustrative example is given on the left-hand side of figure 27. It shows the result of a photoemission calculation by Henk and Johansson [32]. In the centre panel the evolution of theoretical photoemission spectra from Cu(100) for a photon energy of 21.2 eV for a stepwise reduction of the symmetry of the experimental set-up is depicted. The bottom panel (a) shows the corresponding electronic bands along the Δ axis, i.e., for normal emission. Also shown are the relevant final-state bands, shifted down in energy by 21.2 eV. The crossing points of these lines with the initial-state bands determine the positions in k -space where direct transitions will occur.

The bottommost spectrum in the centre panel (b) is for the totally symmetric geometry (figure 11). As outlined in section 4.1, only initial states with an admixture of Δ^5 spatial symmetry contribute to the photoemission signal in that geometry. In figure 27(a), these are the two bands around 2.7 eV binding energy. The next spectrum in panel (b) is calculated for off-normal light incidence under 45° . In that geometry, transitions from states with Δ^1 spatial symmetry are also allowed [42], which give rise to the shoulder in the peak at 3.0 eV binding energy. The third spectrum is for 5° off-normal emission, but normal light incidence. In that case a reflection at the x - z plane reverses the light polarization, keeping everything else constant. This means that according to the considerations of section 3 there is no dichroism. The restriction by the dipole selection rules, however, is lifted for the lower symmetry. For light incidence and emission in mirror planes of the crystal, only selection by the parity of the electronic states persists. Although the electronic states probed at 5° off-normal emission are no longer the ones shown in the bottom panel, the deviation in energy caused by the dispersion of only 5° will not be drastic. It manifests itself in a slight energetic shift of the peak at 2.6 to 2.5 eV binding energy. The more pronounced change is that now substantial emission from the highest-lying band with mainly Δ^2 spatial symmetry at 2.3 eV binding energy is obtained as a consequence of the suspension of the selection rule. The topmost spectrum finally shows the case where neither the light incidence nor the electron emission is along the surface normal. In that case a substantial dichroism D_{pol} is obtained, the asymmetry of which is represented in the top panel (c). The asymmetry is thereby defined as the difference of the two partial spectra normalized to the sum. The dichroism D_{pol} results from the interference due to phase relations between transition matrix elements in the final state [32]. More intuitively it may be regarded as a spin-dependent surface transmission effect, which emerges from the matching condition at the crystal surface for pure spin states on the vacuum side and mixtures of spin-up and spin-down states due to spin-orbit coupling inside the crystal [60]. This is, however, a simplified picture, and not strictly valid in all geometries [61].

Experimental investigations of D_{pol} at Cu(100) revealed an asymmetry of more than 6% [60]. This is about the same magnitude as expected for the 'magnetic' dichroisms D_{ex} and D_{mag} . It is therefore desirable to separate these two effects in order to draw conclusions about the electronic states from off-normal dichroism experiments.

An illustration is given on the right-hand side of figure 27. It shows the influence of lowering the symmetry on calculated photoemission spectra from perpendicularly magnetized Ni/Cu(100). The relativistic band structure (d) and partial photoemission spectra (e) for positive (solid lines) and negative helicity (dotted lines) in the same geometries as on the left-hand side are presented [32]. Note that the bottommost set of spectra (normal incidence, normal

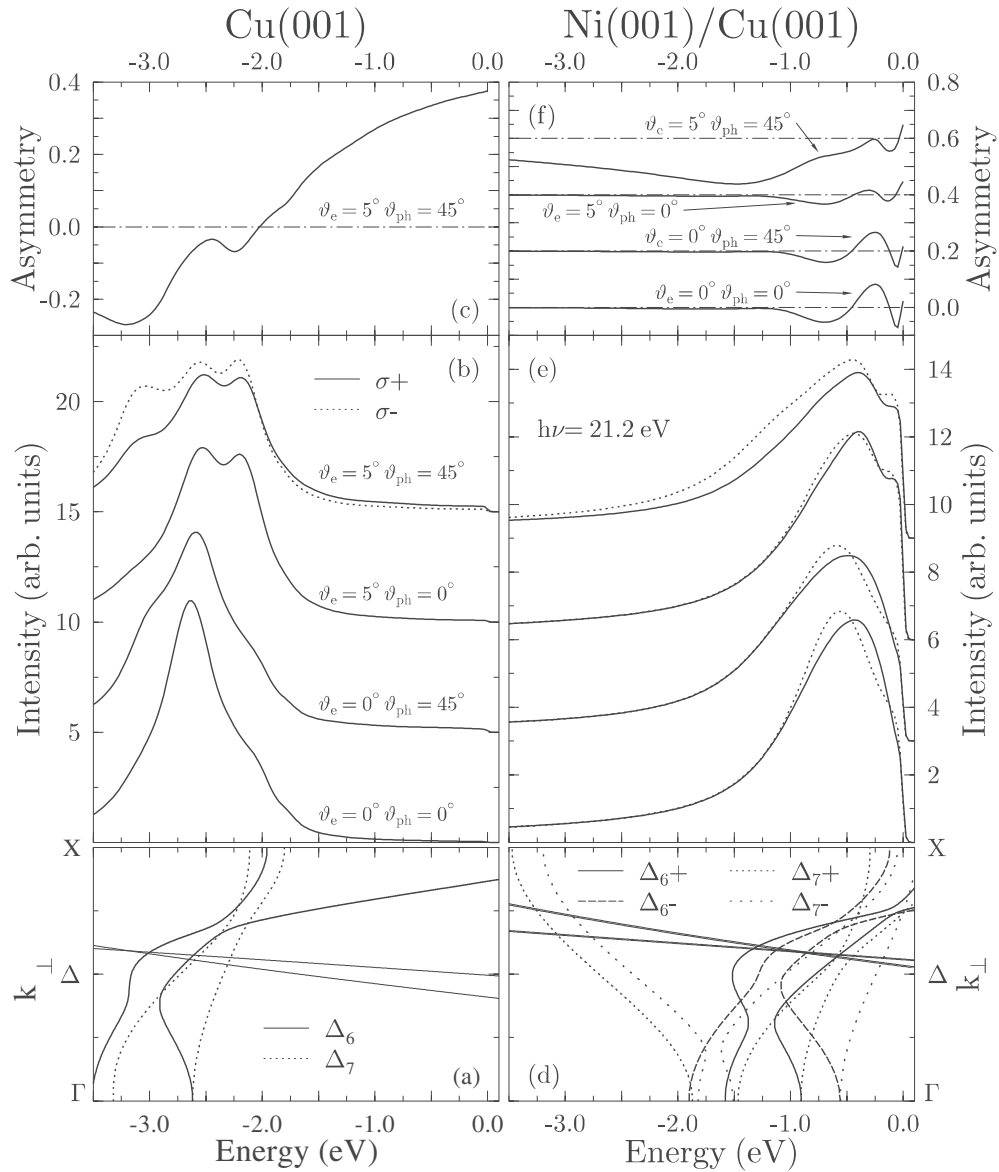


Figure 27. Fully relativistic theoretical band-structure and photoemission calculations for Cu(100) (left), and Ni/Cu(100) (right) by Henk and Johansson [32]. The bottom panels (a) and (d) show the electronic bands along the Δ axis, i.e., for normal emission. Also shown are the relevant final-state bands, shifted down in energy by 21.2 eV. The crossing points of these lines with the initial-state bands determine the positions in k -space where direct transitions will occur. Panels (b) and (e) represent photoemission calculations for a photon energy of 21.2 eV for a stepwise reduction of the symmetry of the experimental set-up. The bottommost spectra are for the totally symmetric geometry (cf. figure 11); above follow spectra for 45° off-normal light incidence and normal emission, for 5° off-normal emission and normal light incidence, and for 5° off-normal emission and 45° off-normal light incidence. The top panels (c) and (f) show the corresponding dichroic asymmetries (defined as the difference of two partial spectra normalized to the sum) in the cases where dichroism occurs. (From reference [32].)

emission) are calculated for experimental conditions identical to those for the spectra already shown in figures 13 and 15, but with a larger imaginary part of the optical potential, which results in a larger broadening of the peaks. Asymmetries corresponding to the four geometrical scenarios of figure 27(e) are reproduced in the topmost panel (f). The strongest effects upon lowering the symmetry of the experiment are observed in the low-symmetry case of off-normal incidence plus off-normal emission, i.e., in the geometry in which a dichroism is present also in the non-magnetic case. Comparing the respective spectra for non-magnetic Cu (figure 27(b)) with the spectrum for Ni/Cu (figure 27(e)), it seems obvious that this strong influence of lowering the symmetry in the magnetic case is caused by the superposition of two effects: the magnetic dichroism, as dealt with in the previous sections and described by spin-orbit- and exchange-split initial states, and the effect of surface transmission, which would be similarly present also without magnetization.

The separation of the experimental dichroism of the theoretical spectra into D_{ex} , D_{mag} , and D_{pol} according to equations (14)–(16) is shown in figure 28(b). It shows the corresponding asymmetries A_{ex} , A_{mag} , and A_{pol} , which are derived from the dichroic differences by normalization to the sum. The four inequivalent partial spectra for the four combinations of helicity and magnetization directions are reproduced in figure 28(a). For a situation like this in which all three types of dichroism D_{ex} , D_{mag} , and D_{pol} (or A_{ex} , A_{mag} , and A_{pol}) are non-zero was termed ‘double dichroism’ in reference [32]. The word ‘double’ implies the presence of two effects, one a final-state effect which would be present also in the non-magnetic case, and a second arising from the simultaneous presence of spin-orbit and exchange interaction in the initial states. In figure 28(b) the dominating influence of A_{pol} , which includes the final-state effects, is clearly seen, and emphasizes the importance of separating initial- and final-state effects.

Venus analytically derived general conclusions for magnetic dichroism in off-normal photoemission for in-plane magnetization [61]. He found that for emission within a mirror plane of the crystal, initial-state effects depend on hybridizations due to spin-orbit coupling in the valence bands. They should contribute positive/negative features to the dichroism. The final-state mechanism, on the other hand, should lead to peaks in the dichroism spectrum of single sign (positive or negative), regardless of whether or not the initial-state band is hybridized [61].

In practice, for the close-lying initial-state bands of a ferromagnetic material, the distinction of overlapping dichroism peaks into single-sign or positive/negative features can be rather difficult for single photoemission spectra [63]. However, in order to map valence bands, usually angle or photon energy series of spectra are acquired. Following in such a series the dispersion of the dichroism peaks facilitates the classification into initial-state and final-state dichroism as defined above [64]. Figure 29 shows as an example a series of photoemission spectra for 5 ML Co/Cu(100) [62]. A geometry similar to the one shown in figure 7 was used. Instead of using the normal-emission geometry of figure 7, the photoelectrons were collected in the x -azimuth in the direction of light incidence, i.e., $\vec{k} = -\vec{q}$. The emission angle with respect to the surface normal \vec{n} is denoted by Θ . The light of 16 eV photon energy is linearly p polarized, and the magnetization direction switched from $+y$ to $-y$ to obtain the dichroism. The left-hand side shows magnetization-averaged photoemission intensity spectra for different angles Θ . Such an angle series resembles the findings of a typical angle-resolved photoemission experiment which is performed to map the band dispersion. However, only very little dispersion is visible from these spectra. From the width of the structures one could infer that more than one transition is involved, but a separation seems impossible. The inelastic background is significantly enhanced for off-normal emission. Obviously much more information is contained in the corresponding dichroic asymmetry spectra, which are shown on the right-hand side. They are obtained from normalizing the difference between

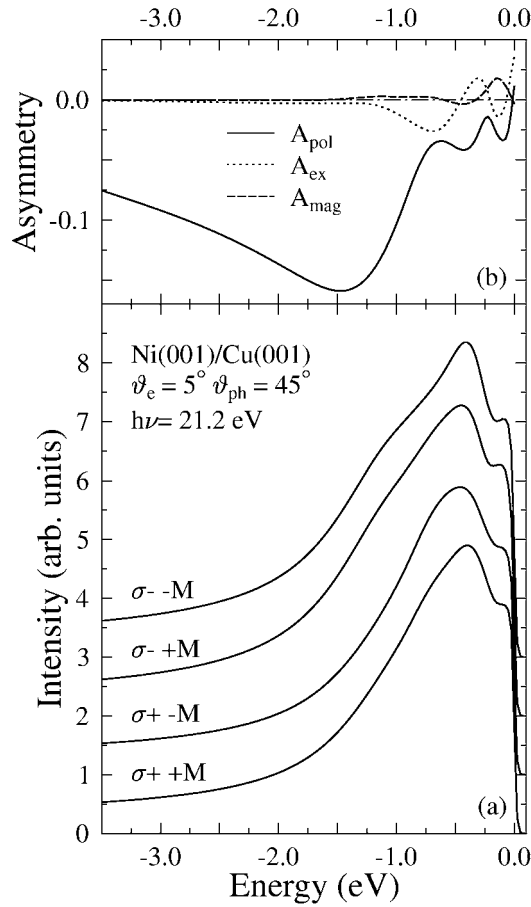


Figure 28. Fully relativistic photoemission calculations of Ni/Cu(100) for 5° off-normal emission and 45° light incidence. (a) The four inequivalent partial spectra which are obtained by changing the directions of the light helicity σ and the magnetization M . (b) Separation of the theoretical dichroism into the asymmetries A_{ex} , A_{mag} , and A_{pol} , corresponding to the differences D_{ex} , D_{mag} , and D_{pol} as defined by equations (14)–(16). (From reference [32].)

spectra with opposite sample magnetization by their sum. Here a pronounced dispersion of various positive/negative features is evident. The presence of significant dichroism in the region between 1 and 2 eV binding energy indicates the presence of magnetic initial-state bands in that region, which are not discernible as peaks in the intensity spectra. This again demonstrates the power of the differential nature of the dichroism in locating transitions from magnetic electronic states under high background or non-magnetic substrate emission.

For the analysis of the data, the dichroism is replotted in figure 30 as a contour plot [62]. Contours of constant positive and negative asymmetry as a function of binding energy and the parallel component of the wavevector k_{\parallel} are represented by solid and dotted lines, respectively. The asymmetry interval between contours is 0.5%. The zero-asymmetry contour line is not plotted. At $k_{\parallel} = 0$ (i.e. $\Theta = 0$, normal emission, and normal incidence) no dichroism is expected in view of the high symmetry (cf. section 3). At binding energies above 2 eV, however, some dichroism is still observed. It has to be attributed to the secondary-electron background, which may produce some false dichroism.

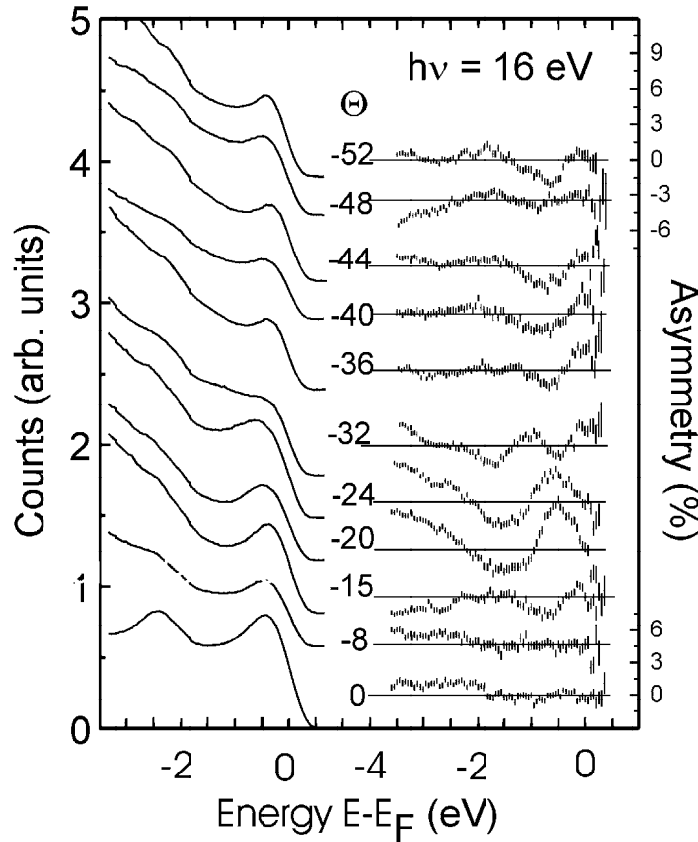


Figure 29. Series of experimental photoemission spectra of 5 ML Co/Cu(100) (left) and magnetic dichroism asymmetry curves (right) for off-normal emission in the direction of light incidence ($\vec{k} = -\vec{q}$) under an angle Θ to the surface normal, excited by linearly p-polarized light of 16 eV photon energy. (From reference [62].)

Unambiguous dispersion of the major regions with positive and negative asymmetry is noticed in figure 30. Approximate lines following maxima and minima of the asymmetry have been sketched in to aid in the discussion of the observed features. The most prominent feature of positive dichroism disperses rapidly from 2 eV binding energy at $k_{\parallel} = -1.0 k_x$ until it crosses the Fermi level at $k_{\parallel} = -0.3 k_x$. k_x here denotes the distance from Γ to X along Δ in the bulk Brillouin zone. The positive maximum is accompanied by a negative peak with an about 0.9–1.2 eV higher binding energy. In addition, two other extrema with a smaller dispersion are traced in figure 30. One crosses the Fermi level at about $-0.6 k_x$ to reach an extrapolated value of 0.2 eV for $k_{\parallel} = 0$, the other, showing negative dichroism, is located at binding energies around 0.6–0.7 eV.

To correlate the maxima and minima in the dichroism spectra with electronic states in the band structure, and to arrive at an experimental band structure, it is in most cases necessary to start from a theoretical band structure as input. As mentioned in the introduction to this section, one drawback of measurements in off-normal emission is that only very few calculations exist for low-symmetry regions of the Brillouin zone. In general it will thus be necessary to perform a band-structure calculation for the specific low-symmetry direction under consideration. Such a (non-relativistic) calculation for the present case is presented in figure 31 [62]. It shows the

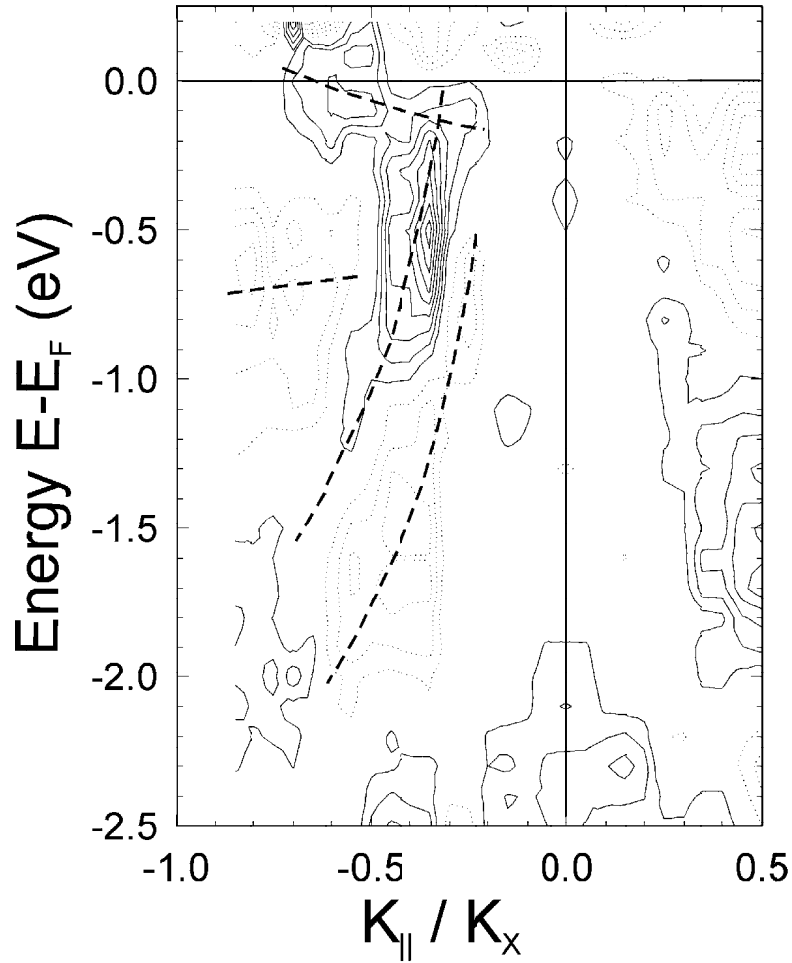


Figure 30. Contours of constant magnetic dichroism interpolated from the data in figure 29 as a function of binding energy and the parallel component of the wavevector k_{\parallel} . Positive (negative) contours are shown as solid (dotted) lines. The asymmetry interval between contours is 0.5%. The zero-asymmetry contour line is not plotted. (From reference [62].)

fcc Co bulk band structure along an axis parallel to Δ , with $k_{\parallel} = 0.35 k_x$. This value of k_{\parallel} corresponds to the highest positive asymmetry, which is observed at $k_{\parallel} = -0.35 k_x$ and 0.5 eV binding energy. The labels 'g' and 'u' on the bands denote even or odd representation of the single group, respectively. The thick solid line in figure 31 represents the relevant pair of final-state bands with negligible exchange splitting, shifted down in energy by the photon energy of 16 eV. Possible transitions from the initial-state bands to these final states in the energy range between E_F and 2 eV binding energy are labelled a to f. Around 0.5 eV binding energy, transitions a–c could be the origin of the observed strong dichroism. The maximum of the negative dichroism, which in the experiment is at about 1.5 eV at $k_{\parallel} = -0.35 k_x$, has to stem from one of the transitions d–f. Under the assumption that the positive and negative maxima with similar dispersion in the asymmetry contour plot (figure 30) correspond to transitions from a pair of exchange-split initial-state bands, transitions b and f could be identified as responsible for these two features [62]. The initial-state energies of these transitions agree

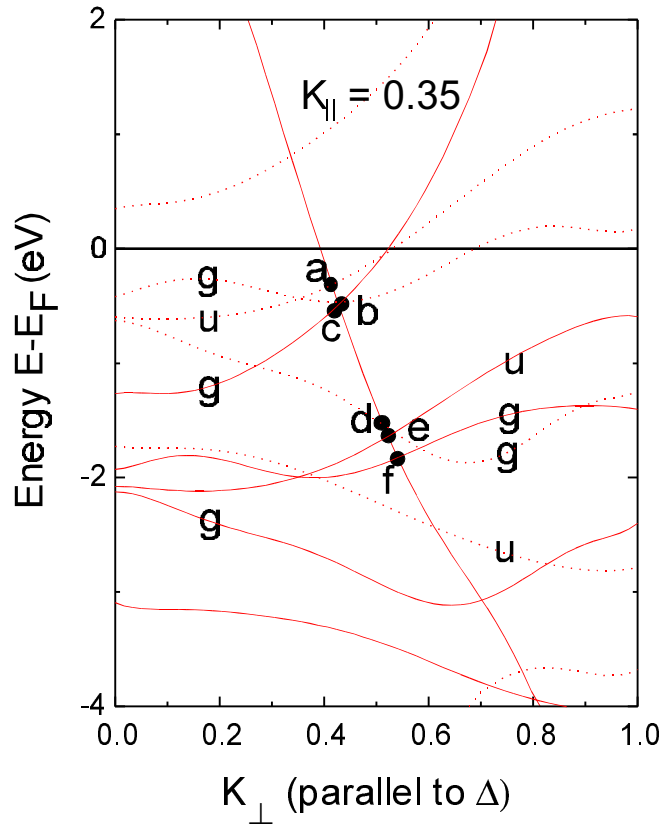


Figure 31. A non-relativistic band-structure calculation for fcc bulk Co along an axis parallel to Δ , with $k_{\parallel} = 0.35 \bar{\Gamma}\bar{X}$. Solid lines indicate majority bands, dotted lines minority bands. Labels ‘g’ (‘u’) on the bands denote even (odd) representation of the single group. The thick solid line represents the relevant pair of final-state bands with negligible exchange splitting, shifted down in energy by the photon energy of 16 eV. Possible transitions from the initial-state bands to these final states in the energy range between the Fermi energy E_F and 2 eV binding energy are labelled a to f. (From reference [62].)

well with the energies at which the two magnetic dichroism extrema in figure 30 cross through $k_{\parallel} = -0.35 k_x$. The dispersing maxima of single sign (positive and negative at the positions of the minority and majority band, respectively) suggest that the magnetic dichroism observed for these bands is probably due to the final-state mechanism [61]. In the picture of direct transitions from bulk-like bands, this would be described as spin-dependent transmission at the surface.

The other two extrema in magnetic dichroism marked by dashed lines in figure 30 may also be interpreted as dispersing initial-state bands. The positive dichroism crossing E_F at about $-0.6 k_x$ could be due to transition a of figure 31. Emission from that band, which has an odd symmetry, would not be observed without spin-orbit-induced hybridization [62]. In fact, hybridization with the majority band constituting transition c would mix in the required parity, and lead to initial-state dichroism. As mentioned before, a positive/negative dichroism should result from that [61]. The convergence of transitions a, b, and c at $k_{\parallel} = 0.35 k_x$ creates overlapping contours of magnetic dichroism from which it is difficult to extract the shape of the individual contributions. However, moving to more negative k_{\parallel} in figure 30, it is evident that

the dispersing negative maximum at -0.7 eV, which merges with the others at $k_{\parallel} = -0.35 k_x$, in fact represents the majority band of even symmetry which leads to transition c.

It should also be mentioned that, although at normal emission no dichroism exists in the geometry of reference [62], an extrapolation of the observed minority and majority features of figure 30 to $k_{\parallel} = 0$ is reasonable. Such an extrapolation yields binding energies of approximately 0.3 and 0.6 eV for minority and majority bands, respectively, which agrees well with spin-resolved photoemission experiments [41].

In conclusion, in the case of magnetic dichroism in off-normal emission also, which is less favourable as regards symmetry-based analysis of direct transitions, an impressive amount of detailed qualitative band-structure information can still be extracted. Because of its differential nature, the magnetic dichroism reveals structure from overlapping transitions even within rather broad photoemission intensity peaks, and also reveals transitions within the large signal of secondary electrons. With the aid of more sophisticated fully relativistic photoemission calculations a more quantitative analysis will be possible, so magnetic dichroism in valence band photoemission even in low-symmetry geometries will be a versatile tool for the study of the electronic structure of ferromagnetic materials.

5. Outlook

In this contribution we intentionally discussed only some selected aspects of magnetic dichroism in angle-resolved valence state photoemission. This was done in order to highlight the basic physical mechanisms and processes involved in this spectroscopic approach. It was our aim to demonstrate that magnetic dichroism can be observed in a large variety of experimental situations and that specific information about the electronic states can be obtained from the photoemission spectra. It is thus justified to view MDAD as a fully developed technique for the analysis of valence electronic states in magnetic materials. From now on it can therefore be employed on a regular basis for the analysis of d- and f-electron states in magnetic bulk crystals and thin epitaxial films, clusters, and artificial nanostructures. In addition to the single-element model systems referred to above, chemically more complex magnetic alloys and compounds will also be of interest in the future. In this case too, MDAD can be expected to yield valuable information about the electronic structure of these materials.

Acknowledgments

We are indebted to R Feder, J Kirschner, D Venus, J Henk, A Rampe, and G Schönhense for fruitful discussions. Thanks go to A Dittschar, M-T Lin, and M Zharnikov for their invaluable collaboration. The work would not have been possible without the help of the BESSY staff, in particular F Schäfers. We acknowledge financial support by the German Ministry of Education and Research (BMBF) through grants No 05 SL8EF1 9 and No 05 SC8BDA 2.

References

- [1] Singh M, Wang C S and Callaway J 1975 *Phys. Rev. B* **11** 287
- [2] Ackermann B, Feder R and Tamura E 1984 *J. Phys. F: Met. Phys.* **14** L173
- [3] Fritsche L, Noffke J and Eckardt H 1987 *J. Phys. F: Met. Phys.* **17** 943
- [4] Ebert H, Strange P and Gyorffy B 1988 *J. Appl. Phys.* **63** 3052
- [5] Kirschner J, Feder R and Wendelken J F 1981 *Phys. Rev. Lett.* **47** 614
- [6] Clauberg R, Gudat W, Kisker E, Kuhlmann E and Rothberg G M 1981 *Phys. Rev. Lett.* **47** 1314
- [7] van der Laan G, Thole B T, Sawatzky G A, Goedkoop J B, Fuggle J C, Esteva J M, Karnatak R, Remeika J P and Dabkowska H A 1986 *Phys. Rev. B* **34** 6529

- [8] Schütz G, Wagner W, Wilhelm W, Kienle P, Zeller R, Frahm R and Materlik G 1987 *Phys. Rev. Lett.* **58** 737
- [9] Baumgarten L, Schneider C M, Schäfers F, Petersen H and Kirschner J 1990 *Phys. Rev. Lett.* **65** 492
- [10] Schneider C M, Hammond M S, Schuster P, Cebollada A, Miranda R and Kirschner J 1991 *Phys. Rev. B* **44** 12 066
- [11] Kirschner J 1985 *Polarized Electrons at Surfaces (Springer Tracts in Modern Physics vol 106)* (Berlin: Springer)
- [12] Kirschner J 1985 *Polarized Electrons in Surface Physics* ed R Feder (Singapore: World Scientific)
- [13] Bassani F and Parravicini G P 1975 *Electronic States and Optical Transitions in Solids* ed R A Ballinger (Oxford: Pergamon)
- [14] Wöhlecke M and Borstel G 1981 *Phys. Rev. B* **23** 980
- [15] Cracknell A P 1975 *Group Theory in Solid-State Physics* (London: Taylor and Francis)
- [16] Eckardt H, Fritsche L and Noffke J 1984 *J. Phys. F: Met. Phys.* **14** 97
- [17] Schneider C M and Kirschner J 1995 *Crit. Rev. Solid State Mater. Sci.* **20** 179
- [18] Eyers A, Schäfers F, Schönhense G, Heinzmann U, Oepen H P, Hünlich K, Kirschner J and Borstel G 1984 *Phys. Rev. Lett.* **52** 1559
- [19] Oepen H P, Hünlich K, Kirschner J, Eyers A, Schäfers F, Schönhense G and Heinzmann U 1985 *Phys. Rev. B* **31** 6846
- [20] Tamura E, Feder R, Vogt B, Schmiedeskamp B and Heinzmann U 1989 *Z. Phys. B* **77** 129
- [21] Schneider C M, Garbe J, Bethke K and Kirschner J 1989 *Phys. Rev. B* **39** 1031
- [22] Oepen H P, Hünlich K, Kirschner J, Eyers A and Schäfers F 1986 *Solid State Commun.* **59** 521
- [23] Oepen H P, Hünlich K and Kirschner J 1986 *Phys. Rev. Lett.* **56** 496
- [24] Garbe J and Kirschner J 1989 *Phys. Rev. B* **39** 9859
- [25] Tamura E, Piepke W and Feder R 1987 *Phys. Rev. Lett.* **59** 943
- [26] Tamura E and Feder R 1991 *Europhys. Lett.* **16** 695
- [27] Tamura E and Feder R 1991 *Solid State Commun.* **79** 989
- [28] Schmiedeskamp B, Vogt B and Heinzmann U 1988 *Phys. Rev. Lett.* **60** 651
- [29] Schmiedeskamp B, Irmer N, Vogt B and Heinzmann U 1991 *Appl. Phys. A* **53** 418
- [30] Irmer N, David R, Schmiedeskamp B and Heinzmann U 1992 *Phys. Rev. B* **45** 3849
- [31] Falicov L and Ruvalds J 1968 *Phys. Rev.* **172** 498
- [32] Henk J and Johansson B 1998 *J. Electron Spectrosc. Relat. Phenom.* **94** 259
- [33] Schulz B and Baberschke K 1994 *Phys. Rev. B* **50** 13 467
- [34] Bocchi G, Ballentine C A, Ingelfield H E, Thompson C V, O'Handley R C, Hug H J, Stiefel B, Moser A and Güntherodt H-J 1995 *Phys. Rev. B* **52** 7311
- [35] Shen J, Giergiel J and Kirschner J 1995 *Phys. Rev. B* **52** 8454
- [36] Wu S Z, Mankey G J and Willis R F 1995 *J. Vac. Sci. Technol. A* **13** 1497
- [37] Kuch W, Dittschar A, Meinel K, Zharnikov M, Schneider C M, Kirschner J, Henk J and Feder R 1996 *Phys. Rev. B* **53** 11 621
- [38] Müller S, Schulz B, Kostka G, Farle M, Heinz K and Baberschke K 1996 *Surf. Sci.* **364** 235
- [39] O'Brien W L, Droubay T and Tonner B P 1996 *Phys. Rev. B* **54** 9297
- [40] Hjortstam O, Baberschke K, Wills J M, Johansson B and Eriksson O 1997 *Phys. Rev. B* **55** 15 026
- [41] Schneider C M, de Miguel J J, Bressler P, Schuster P, Miranda R and Kirschner J 1990 *J. Electron Spectrosc. Relat. Phenom.* **51** 263
- [42] Eberhardt W and Himpsel F J 1980 *Phys. Rev. B* **21** 5572
- [43] Kuch W, Lin M-T, Meinel K, Schneider C M, Noffke J and Kirschner J 1995 *Phys. Rev. B* **51** 12 627
- [44] Scheunemann T, Halilov S V, Henk J and Feder R 1994 *Solid State Commun.* **91** 487
- [45] Henk J, Scheunemann T, Halilov S V and Feder R 1996 *J. Phys.: Condens. Matter* **8** 47
- [46] Kuch W, Zharnikov M, Dittschar A, Meinel K, Schneider C M, Kirschner J, Henk J and Feder R 1996 *J. Appl. Phys.* **79** 6426
- [47] Kuch W, Dittschar A, Zharnikov M and Schneider C M 1996 unpublished
- [48] Kuch W, Dittschar A, Salviotti M, Lin M-T, Zharnikov M, Schneider C M, Camarero J, de Miguel J J, Miranda R and Kirschner J 1998 *Phys. Rev. B* **57** 5340
- [49] de la Figuera J, Prieto J E, Ocal C and Miranda R 1993 *Phys. Rev. B* **47** 13 043
- [50] Kief M T and Egelhoff W F Jr 1993 *Phys. Rev. B* **47** 10 785
- [51] Miranda R 1993 *Phys. Scr. T* **49** 579
- [52] Huang F, Kief M T, Mankey G J and Willis R F 1994 *Phys. Rev. B* **49** 3962
- [53] Camarero J, Graf T, de Miguel J J, Miranda R, Kuch W, Zharnikov M, Dittschar A, Schneider C M and Kirschner J 1996 *Phys. Rev. Lett.* **76** 4428
- [54] Camarero J, Spendeler L, Schmidt G, Heinz K, de Miguel J J and Miranda R 1994 *Phys. Rev. Lett.* **73** 2448
- [55] Ebert H 1991 private communication

- [56] Rampe A, Güntherodt G, Hartmann D, Henk J, Scheunemann T and Feder R 1998 *Phys. Rev. B* **57** 14 370
- [57] Fanelsa A, Kisker E, Henk J and Feder R 1996 *Phys. Rev. B* **54** 2922
- [58] Bansmann J, Lu L, Getzlaff M and Meiwes Broer K H 1997 *Surf. Sci.* **377–379** 476
- [59] Bansmann J, Getzlaff M, Schönhense G, Fluchtman M and Braun J 1998 *Surf. Sci.* **402–404** 365
- [60] Venus D, Kuch W, Dittschar A, Zharnikov M, Schneider C M and Kirschner J 1995 *Phys. Rev. B* **52** 6174
- [61] Venus D 1997 *J. Magn. Magn. Mater.* **170** 29
- [62] Venus D, Kuch W, Lin M-T, Schneider C M, Ebert H and Kirschner J 1997 *Phys. Rev. B* **55** 2594
- [63] Venus D, Kuch W, Dittschar A, Zharnikov M, Schneider C M and Kirschner J 1996 *J. Appl. Phys.* **79** 6504
- [64] Venus D 1997 *Phys. Rev. B* **56** 2661